Observation of Gamma Ray with 7m Cherenkov Telescope in Sub TeV Region

Junko Kushida

98M01164

Master Thesis

Department of Physics

Graduate School of Science and Engineering

Tokyo Institute of Technology

February 14, 2000

Abstract

In order to exploit new gamma-ray astronomy in sub-hundred GeV region, a new 7m imaging Cherenkov telescope of CANGAROO (Collaboration of Australia and Nippon(Japan) for a Gamma-Ray Observatory in the Outback) has been started to operate at Woomera, South Australia in May 1999. It has a 7m parabolic mirror consisting of 60 small plastic spherical mirrors, and the prime focus is equipped with a multi-pixel camera of 512 photomultiplier tubes covering the field of view of 3 degrees. This telescope is characterized by using timing information for the rejection of sky background and hadron showers and having the finest pixel size in camera.

We observed some candidates for gamma-ray sources and calibrated the experimental apparatus using these observed and simulated data. Since we use Cherenkov imaging technique to separate gamma rays from background events made by cosmic-ray, determination of energy threshold is essential. The energy threshold of the telescope is determined by using the simulation of Cherenkov technique. Therefore it is important to estimate of each parameter used here. Comparing the single count rate of each PMT for observed data with that expected for night sky background light, hit threshold levels of updating and non-updating discriminator for PMTs was estimated about 3 photoelectrons and about 4 photoelectrons. Using this result, the threshold energy for hadron shower was estimated to be less than 800 GeV and the threshold energy for gamma-ray was expected to be $200 \sim 300$ GeV, which are well consistent with the estimated from the spectrum of observed cosmic rays.

For the purpose of examining the performance of 7m telescope, the Crab nebula, which is the standard candle of TeV gamma-ray emission, was observed with 7m telescope in December 1999 and January 2000 at the large zenith angle of 55°. Total observation times are 39 hours for on-source and 31 hours for off-source. A positive gamma-ray signal looks to be found in the analysis, though it is not significant statistically.

Contents

List of Figures

List of Tables

Chapter 1

Introduction

1.1 History

Gamma-ray astronomy is a quickly developing field. In 1960s, gamma-ray emission to the region of $\sim$ 100 MeV was observed by balloon-bone and rocket experiments. The SAS-II and COS-B satellite experiments launched in the 1970s presented the first significant high energy gamma-ray detections. These experiments, operating at energies between 35 MeV and 5 GeV, found the diffuse gamma-ray concentrating at the galactic plane, and the isotropic extra galactic gamma-ray radiation. Also they detected 25 gamma-ray point sources including the Crab and Vela pulsars.

In 1991, *CGRO* (Compton Gamma Ray observatory) was launched and brought us more interesting information. *CGRO* carried four gamma-ray experiments: EGRET, BATSE, OSSE, and COMPTEL. These experiments cover different energy bands. In particular, EGRET (Energetic Gamma-Ray Experiment Telescope) detects gamma rays in the 20 MeV to 30 GeV range. It is made up of a spark chamber system to track the electron-positron pairs converted from gamma rays and the total absorption calorimeter made of NaI sintillator to measure the energies. According to the third EGRET catalog [11], EGRET has found 271 gamma-ray sources : 5 pulsars, 1 solar flare, 66 high-confidence blazar identifications, 27 possible blazar identifications, 1 likely radio galaxy (Cen A), 1 normal galaxy (LMC), and 170 unidentified sources, which are plotted in Fig. 1.1. Many of unidentified sources are

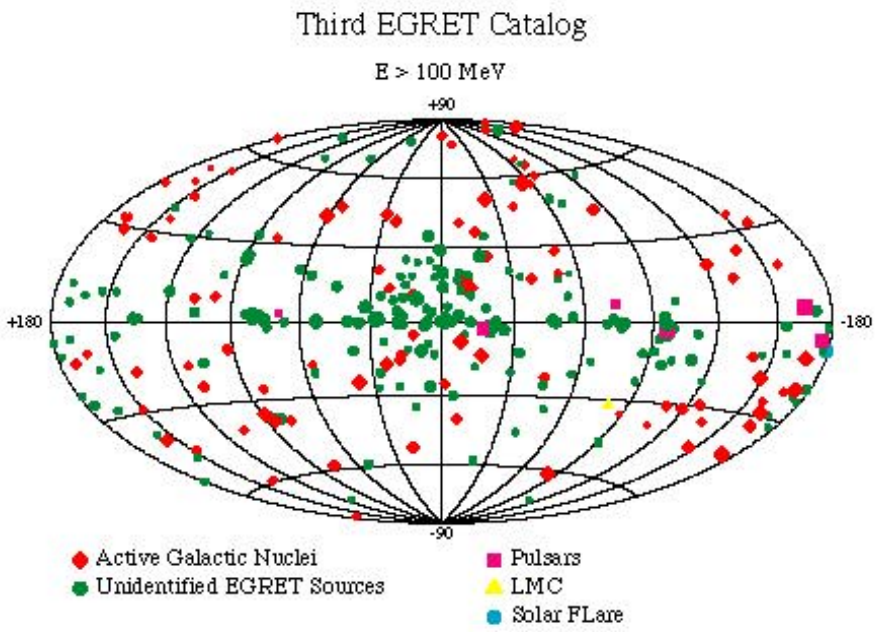

Figure 1.1: Gamma-ray sources map

distributed along the galactic plane and probably associated with pulsars or SNRs.

More energetic gamma rays can be observed with ground-based detectors. From 1960s to 1970s, a number of atmospheric Cherenkov telescopes and air shower arrays operated all over the world. Those used air shower techniques (See Chapter 2). In the early years, since the angular resolution of ground-based detectors was not enough (about one degree), dominant cosmic rays overwhelm gamma-ray signals and no trust worth source was found. The Whipple observatory developed the imaging technique, in order to distinguish gamma ray from huge backgrounds of hadronic shower events. Using the imaging technique, six TeV gamma-ray sources have been found by ground-based telescopes until now. (See Fig. 1.2).

However no telescope and satellite has operated in the energy region between 20 and 250 GeV. Next generation ground-based detectors and satellite experiments aim to observe in this regions.

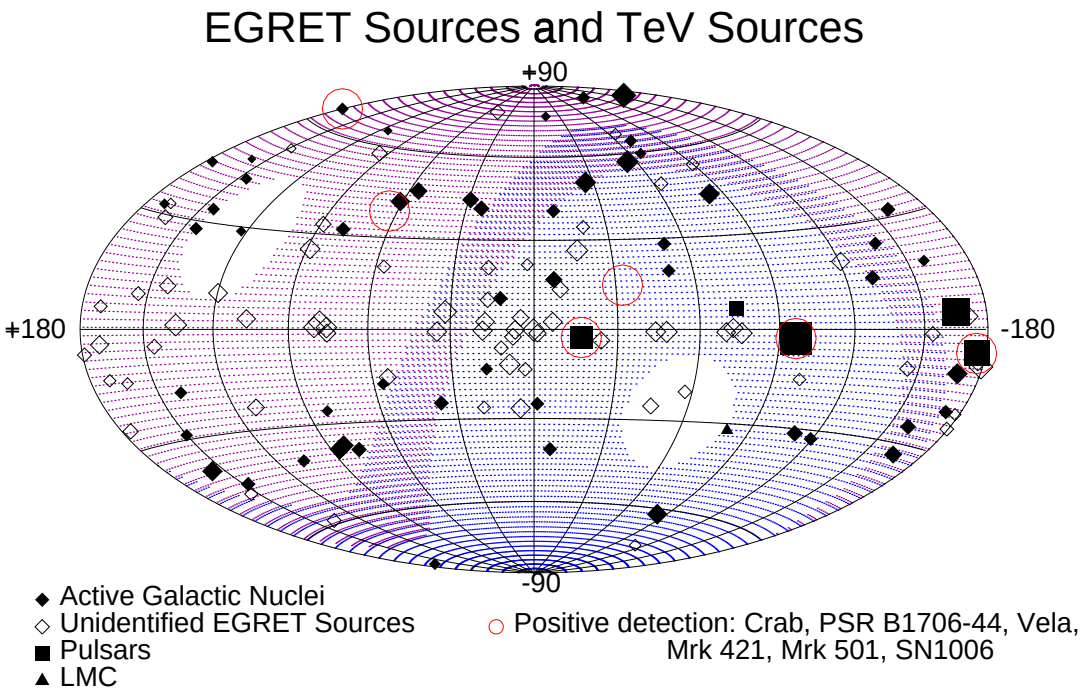

Figure 1.2: TeV and GeV Gamma-ray sources map

Chapter 2

Atmospheric Air Shower Technique

Very high energy gamma rays are detected by ground-based instruments using the Earth's atmosphere as the detection medium. In this chapter, the techniques of ground-based gamma-ray observation are described.

2.1 Air Shower

A very high energy gamma ray entering the earth's atmosphere interacts with molecules in the upper atmosphere at altitudes between 10 and 15 km. The electron-positron pair produced from this interaction initiates an electro-magnetic cascade. It causes bremsstrahlung and emits gamma rays. which also create subsequent pairs.

In this extensive air shower (EAS) process (See Fig. 2.1), the energy of the primary gamma ray is divided into particles, and the average particle energy decreases as the cascade proceeds. Finally, ionization loss becomes dominant for the particles and the cascade will terminate. EAS initiated by hadronic cosmic rays are similar in many respects to those initiated by gamma rays. The initial interaction of a cosmic ray in the atmosphere produce primarily hadronic particles (nuclei, pions, etc). Charged those feed the hadronic cascade, but neutral pions decay into gamma rays as $\pi^0 \rightarrow 2\gamma$s within 10^{-16}sec, and gamma rays initiate electromagnetic sub-showers.

There are several important differences in the development of EAS between gamma-ray

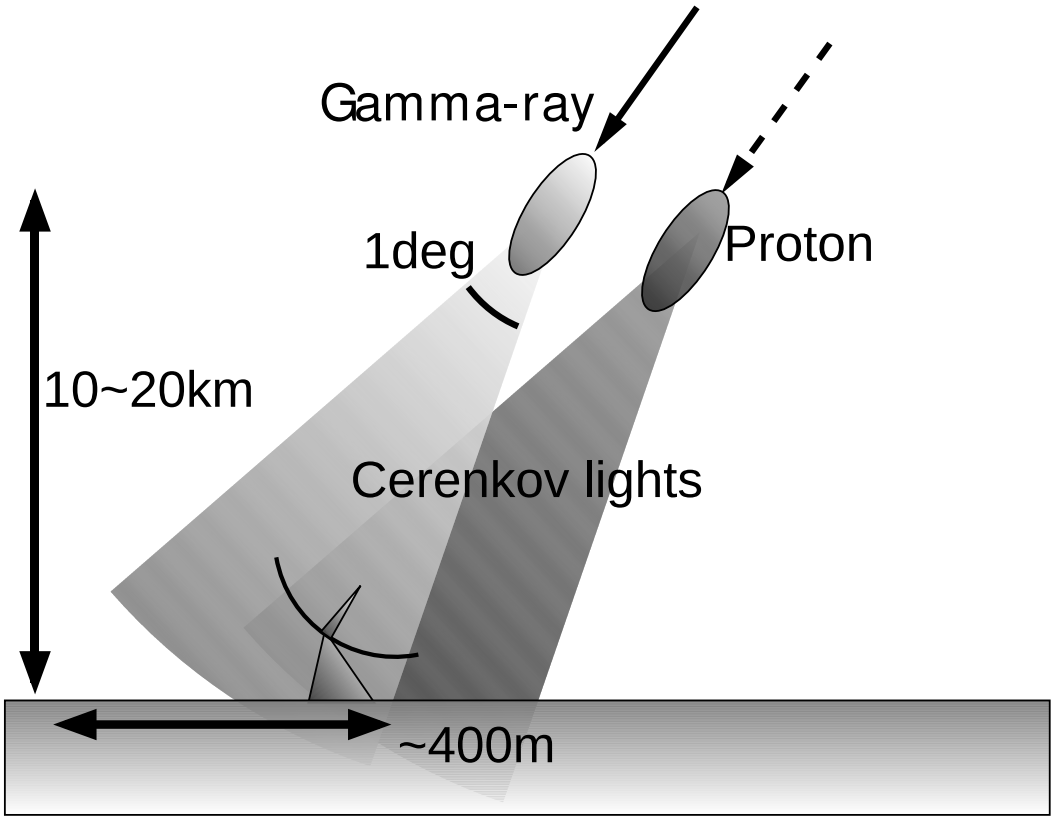

Figure 2.1: The extensive air showers process.

showers and hadronic showers. First, hadronic showers develop later because of the longer interaction length. Second, nuclear cascades have larger transverse momenta than electromagnetic cascades. As shown in Fig. 2.2, hadronic showers are extended more transversely than gamma-ray showers. These two facts also mean that there are larger fluctuations in the development of hadronic showers. Finally, the number of particles in an hadron shower is roughly one third of those of gamma-ray showers because pion of all charges are produced in almost equal numbers in multiparticle production, and hadronic showers have more muons.

2.2 Cherenkov Radiation

A charged particle moving at a velocity $v > c'$ in the medium radiates Cherenkov photons. In a medium of a refractive index n, the velocity of light is $c' = c/n$, where c is the light velocity in a vacuum. The radiation is only permitted at a particular angle θ ("Cherenkov angle") with respect to the track of the particle.

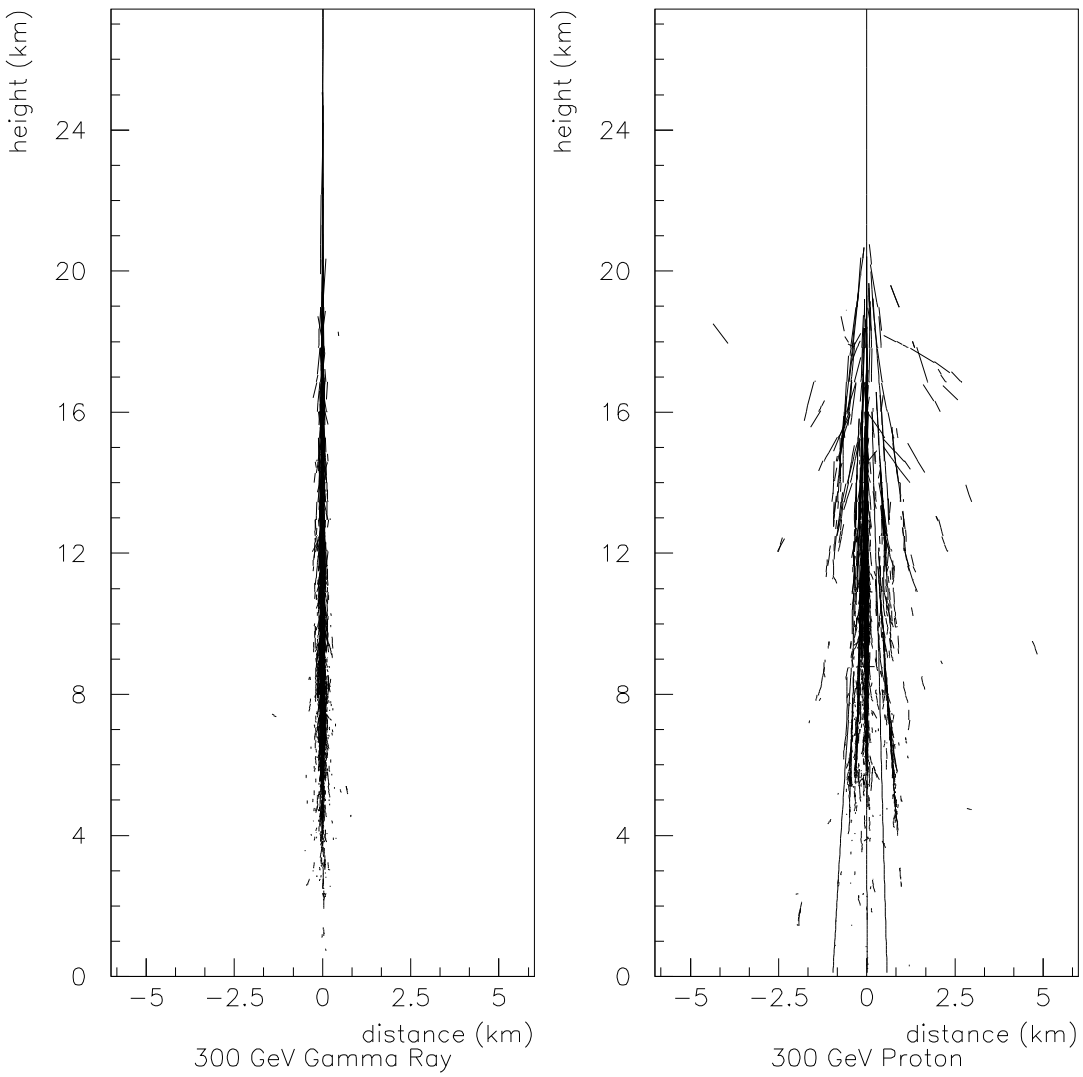

Figure 2.2: Development profiles of Monte Carlo simulated EASs from a 300 GeV gamma ray (left) and a 300 GeV proton (right).

$$\cos\theta = \frac{1}{\beta n} \tag{2.1}$$

with $\beta = v/c$. For the wavelength of 400nm, The refractive index of air at temperature of T° K° is defined in the following way:

$$n = 1.0 + 0.000296 \, \frac{x}{1030\,\mathrm{g\,cm^{-2}}} \frac{\mathrm{T}}{273.2\,\mathrm{K}}^{-1} \tag{2.2}$$

where x is the atmospheric depth in g/cm^2 and T is the atmospheric temperature expressed as T= 204 + 0.091 x [3] . Since $n \sim 1.00027$ at 1 atm, the Cherenkov angle is $\theta \leq 1°.3$ for relativistic particles ($\beta \sim 1$) in an EAS from (2.1). Therefore Cherenkov radiation from the EAS is radiated in a few degrees with respect to the shower axis.

The energy output of Cherenkov radiation from the EAS can be expressed as

$$\frac{dE}{dl} = \frac{Z^2 e^2}{c^2} \int_{\beta n > 1} (1 - \frac{1}{\beta^2 n^2}) \omega \, d\omega \tag{2.3}$$

where Ze is the particle charge and ω is the frequency of Cherenkov radiation [6]. From (2.3), the number of photons radiated into the wavelength range between λ_1 and λ_2 is

$$N = 2\pi\alpha Z^2 l (\frac{1}{\lambda_1} - \frac{1}{\lambda_2})(1 - \frac{1}{\beta^2 n^2}), \tag{2.4}$$

where $\alpha = e^2/\hbar c \simeq 1/137$ is the fine structure constant. The total number of Cherenkov photons radiated from an EAS is proportional to the number of electrons in the EAS. and as mentioned above, the number of Cherenkov photons from a gamma-ray shower is three times of that from a hadronic shower. The lateral distribution of Cherenkov light initiated by a gamma rays is almost flat out to a $\sim$ 150m radius at sea level as shown in Fig. 2.3 and the detection area reaches the order of 10^4m. Moreover, the Cherenkov photon density detected at sea level are approximately proportional to a primary gamma-ray energy within this radius, and becomes a good estimator for the primary gamma-ray energy.

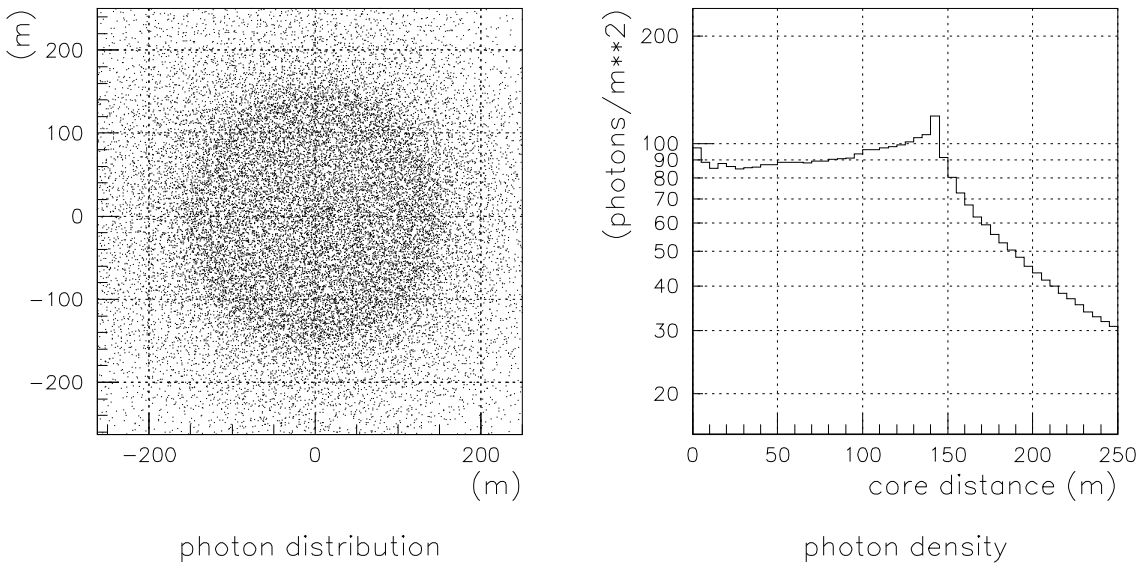

Figure 2.3: Lateral distribution of Cherenkov light from a shower generated by 1 TeV gamma ray at sea level [27].

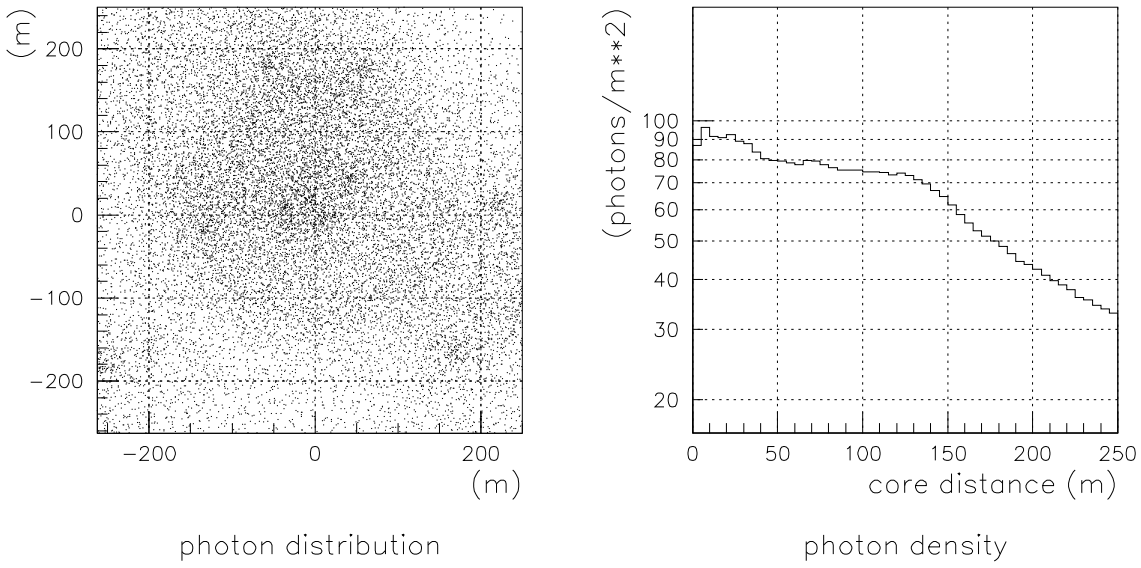

Figure 2.4: Lateral distribution of Cherenkov light from a shower generated by 3 TeV proton at sea level [27].

2.3 Imaging Technique

Atmospheric Cherenkov telescopes detect not only gamma rays but also huge cosmic rays. Therefore, it is important to eliminate background events for effective detections of gamma rays. "Imaging technique" has been well known powerful for rejecting background events. In this technique, Cherenkov images on the focal plane are recorded with an imaging camera consisting of many photomultiplier tubes (PMTs), and the images well reflect the profile of the development of the EAS. The principle of imaging Cherenkov technique is shown in Fig. 2.5.

Since there are differences in the development between EASs initiated by gamma rays and by cosmic-rays, Cherenkov images on the focal plane also reflect these difference. Then Cherenkov images of gamma rays can be distinguished from that of cosmic-rays. Figure 2.6 shows differences of Cherenkov images between an 1 TeV gamma ray and a 3 TeV proton. Gamma-ray images elongate to the source in the field of view. On the other hand, hadronic images have random directions in the field of view reflecting the random directions of the

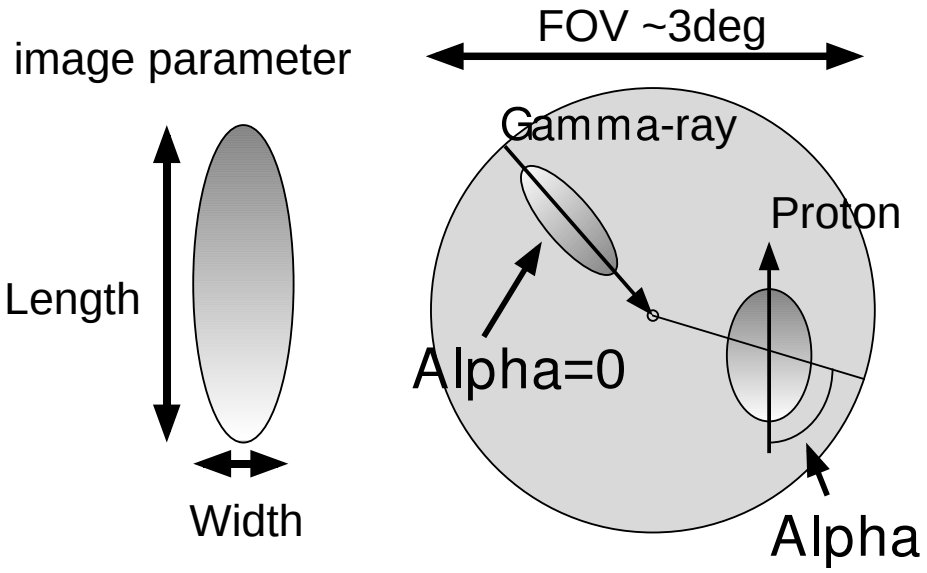

Figure 2.5: The principle of the parameterization of the Cherenkov imaging technique. Gamma-ray images elongate the shower axis in the direction to the object, pointed by telescope.

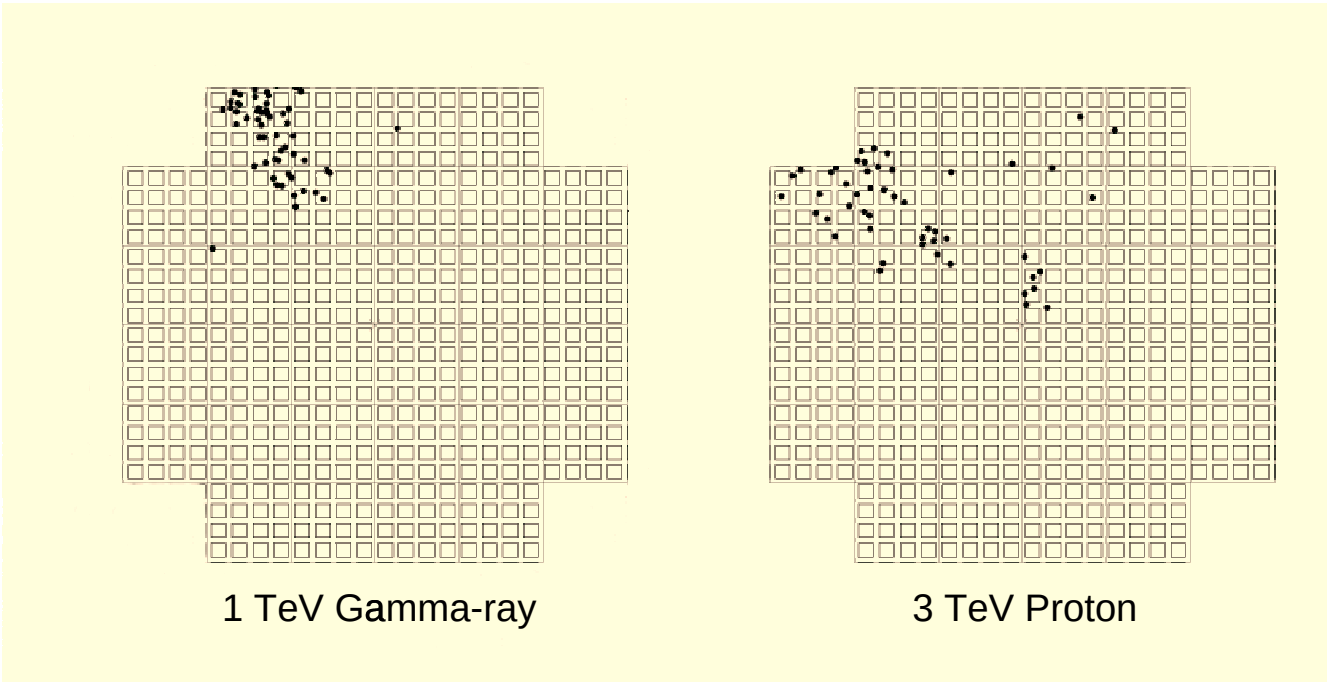

Figure 2.6: Typical Cherenkov images of a 1 TeV gamma ray (left) and a 3 TeV proton (right).

primary nuclei and the irregularity of the shower development.

In the imaging technique, Hillas (1985) has shown that a parameterization based on fitting an ellipse to the Cherenkov images is effective in extracting the characteristics required to enhance gamma-ray signals [4]. The image parameters generally used in the imaging technique are as follows, and schematically shown in Fig. 2.7.

Width The root mean square (RMS) spread of light along the minor axis of the image, a measure of the lateral development of the cascade.

Length The RMS spread of Cherenkov photons along the major axis of the image, a measure of the vertical development of the cascade.

Distance The distance between the centroid of the image and the source position.

Conc The parameter representing the light concentration in the particular part of an image, as determined from the ratio of the several largest tube signals to the sum of all signals.

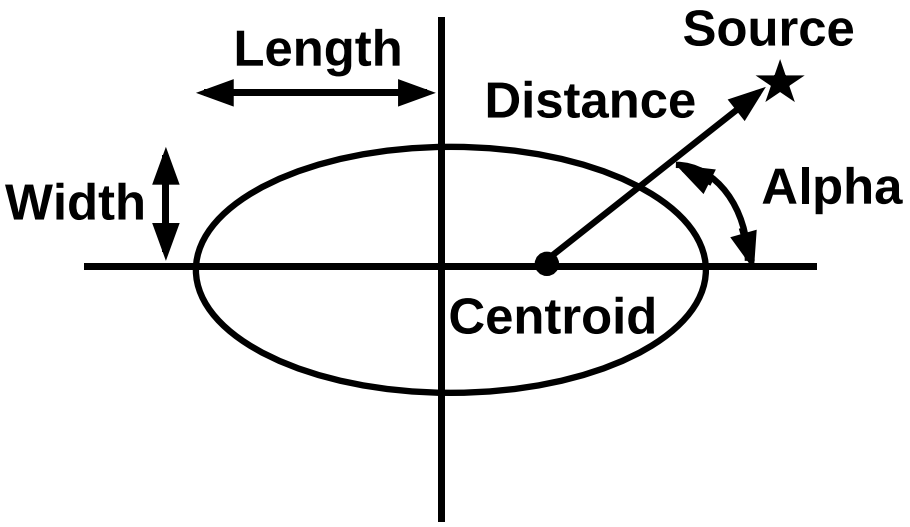

Figure 2.7: Definition of image parameters.

Alpha The angle between the major axis and a line joining the centroid of the image to the source.

Gamma-ray images are actually asymmetrical along their major axes since they elongate toward the opposite side against the source position in the field of view. Asymmetry represents how asymmetric the photon distribution on the image along the major axis. The location of the peak intensity of Cherenkov photon is rather shifted to the source from the image centroid for the gamma-ray image [7]. The "Asymmetry Vector" $\vec{A}$ is defined so as to point towards the source position from the centroid and have a length equal to the cubic root of the third moment of the image along the major axis, since the asymmetry of the photon density is reflected in its odd moments. The vector is schematically shown in Fig.2.8.

If $\vec{D}$ is an distance vector pointing from the image centroid to the assumed source, Asymmetry normalized by Length is given as

$$Asymmetry = \frac{\vec{A} \cdot \vec{D}}{\text{Distance Length } \cos(\text{Alpha})}. \tag{2.5}$$

Asymmetry distribution of Cherenkov images simulated are shown in Fig.2.9 The distribution of gamma-ray images is well one-sided and concentrated around Asymmetry=1, while the distribution of background (proton) images is almost symmetrical since the directions of the simulated primary protons are isotropic.

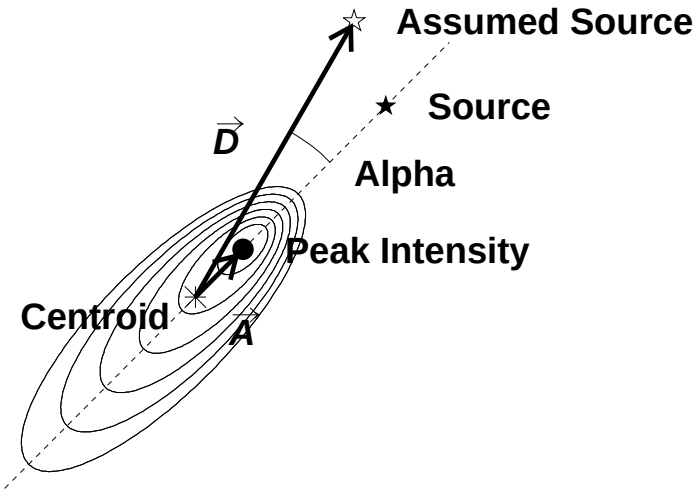

Figure 2.8: Schematic diagram of a typical gamma-ray image to define Asymmetry Vector [29].

The simulated distributions of the above parameters for primary gamma rays and primary protons are shown in Fig.2.9. The Monte Carlo simulation was carried out assuming the primary directions to be of a point source for gamma rays while isotropic for protons. Hadronic images should generally be broader in Width, longer in Length,wide-spread development of their showers. Alpha values of gamma-ray images should be concentrated near Alpha=0°, while Alpha of gamma-ray images should be uniform.

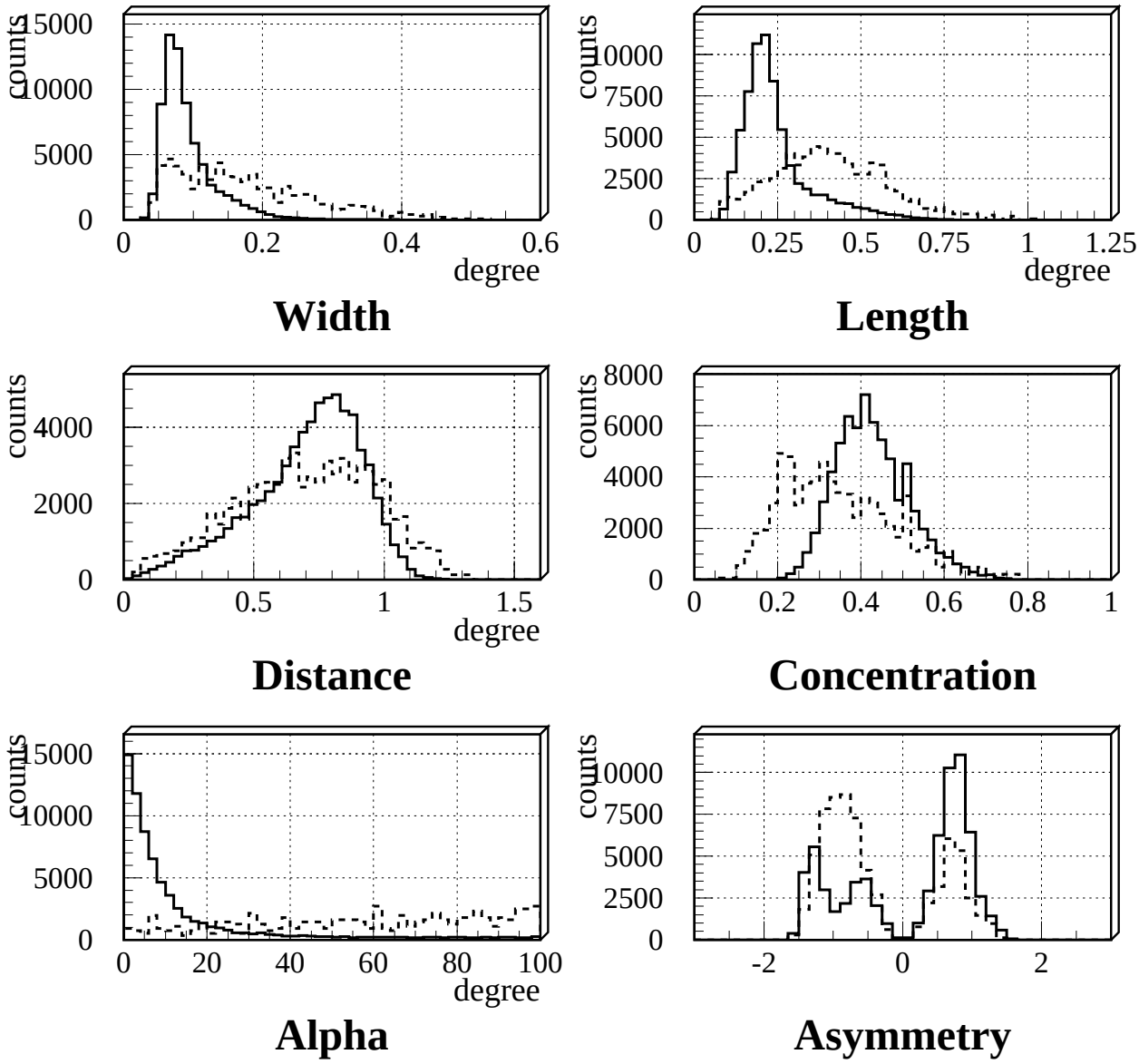

Figure 2.9: Image parameter distributions calculated by Monte Carlo simulation. Gamma-ray source (solid line) and protons (dashed line) for PSR 1706-44.

2.4 Monte Carlo Simulation of Atmospheric Cherenkov Light

For the Monte Carlo simulations both of gamma ray and cosmic ray air showers, we use GEANT utility version 3.15 [10]. GEANT is a system of detector descriptions and the simulation tools for high energy particle physics, which was developed in CERN. We described the atmosphere as a particle calorimeter consisting of 160 air layers, in which the US standard atmospheric structure was used to calculate the air density. Cherenkov photons are produced from each particle generated by GEANT. Numbers of photons hitting PMTs are calculated using the equation (2.3) assuming that the quantum efficiency of the PMTs is constant ($\sim$ 20%) in the wavelength region from 350 nm to 600 nm. The numbers of Cherenkov photons were further been reduced taking the Rayleigh and Mie scattering into account [2]. Generated Cherenkov photons were at first collected by one reflector within simulated area on the ground at sea level. The reflector is assumed to consist of 60 spherical mirrors and to be 7m in diameter. The reflectivity assumed here is 75 %.

Generated photons were modified at the mirror taking into account the blur of the mirror, where the actually measured value for stars was used. Next, an image was reconstructed on the focal plane, and examined about the satisfaction of trigger criteria described in section 3.5. Also the effect of NSB was included here. The simulated images are fed to the same program used in the analysis of real data.

The Monte Carlo simulation of proton showers was also done and the results was checked for the compatibility with the observation data in the triggering rate and the parameter distributions. Primary gamma rays were simulated under the following conditions, and the cosmic ray backgrounds were assumed to be solely protons in this simulation. Simulated primary gamma rays are injected from the direction of the PSR 1706-44 (the Crab nebula). The gamma-ray showers were simulated in the energy range from 100 GeV to 1 TeV (500 GeV to 8 TeV) with the primary differential power of -2.5. and the protons were simulated in the energy range from 200 GeV to 6 TeV (1 TeV to 16 TeV) with power index of -2.7.

The primary directions of protons was distributed uniformly in the 3° radial field, which is about four times larger than the field of view of the camera, and the shower axes were also distributed uniformly in the circle of less than 180m (320m) from the telescope, which is much larger than the effective detection area, and gamma-ray showers were also injected within the circle of 320m, which was large enough for the effective detection as shown in Fig. 2.3 and 2.4.

Chapter 3

Status of the 7m Telescope

3.1 Overview

An international collaboration, CANGAROO (the Collaboration of Australia and Nippon for a Gamma-Ray Observatory in the Outback), between a group of institutions in Japan and the University of Adelaide in Australia was proposed in 1988 and started in 1991. Our group has observed southern gamma-ray sources with an energy threshold of 2 TeV using the 3.8m Cherenkov telescope in Woomera (136 47' E, 31 06' S). Until now CANGAROO group has detected following TeV gamma-ray sources: the Crab nebula, Vela pulsar, PSR 1706-44, and SN1006.

In order to exploit the observation in sub-hundred GeV region, New 7m telescope has constructed in March 1999 near the 3.8m telescope (See Fig.3.1), and operated in June 1999. The characteristics of the 3.8m and 7m telescope are summarized in Table 3.1.

3.2 Mirror

The reflector has a parabolic shape (F/1.1) with the diameter of 7m. in order to use timing information for the rejection of NSB. Other imaging atmospheric Cherenkov telescopes use a Davies-Cotton type reflector in which identical spherical mirrors are mounted on a spherical structure whose curvature radius is exactly a half of the mirrors. Devis-Cotton

Table 3.1: The comparison of characteristics of 3.8m and 7m telescope [13].

	3.8m telescope	7m telescope
Mirror material	Aliminized duralumin	Carbon Fiber Reinforced Plastic (CFRP)
Shape of mirror	Parabolic	Parabolic
Diameter	3.8m	7.2m
Focal length	3.8m	8m
Area	11.3 m^2	30 m^2
Segment		80cm diameter spherical mirror
Pixel size	$0^\circ.12 \times 0^\circ.12$ (square)	$0^\circ.115 \times 0^\circ.115$ (circle),
Point image size		$0^\circ.14$ (FWHM)
Number of pixels	220	512
Total field of view	$\sim 3^\circ$	$\sim 4^\circ$
Tracking accuracy	$\sim 0^\circ.01$	$\sim$ 1arcmin

Figure 3.1: CANGAROO II 7m telescope

type reflectors surpass parabolic design in the off-axis focusing property, but cannot use the timing information.

The surface area of the reflector consists of 60 spherical 80cmϕ small mirrors, and the effective light collecting area is 30 m^2. The curvature radii of small mirrors are distributed between 15.9 to 17.1m (designed value 16.4m). These mirrors were arranged from the inner to the outer taking account of the distributions their curvature radii. This spherical mirror is made of CFRP (Carbon Fiber Reinforced Plastics), to obtain a light and durable mirror. The reflectivity is always kept $\geq$ 80 % in visible band. Since the telescope has no shelter, the mirror surface is damaged by dust and rain. After several months, the reflectivity fell off about 75 %. However the reflectivity can recovers to near 80 % by water washing.

Each mirror is remotely adjusted in two perpendicular directions by using stepping motors which are installed in the back of the mirror. Four shafts support the boss: two shafts are driven by two stepping motors. and the other two shafts with springs firmly fix the attitude. The minimum step size of motor is about 1×10^{-4} degree at the focal plane. All small mirrors are adjusted one by one using two motor drivers with relay switches controlled by a computer. After the first adjustment work, the deviation of mirrors axis orientations is $0^\circ.03$ on average [14]. Figure 3.2 shows the on-axis image of Sirius of which image size is $0.^\circ$ 14(FWHM). A square is superimposed to show the scale of a camera pixel. Thus, $30 \pm 4\%$ of the photons are concentrated in a single camera pixel. The detail of the performance of the reflector will be described in Kawachi et al [15].

3.3 Camera

The imaging camera at focal plane of the telescope consists of 512 photo-multiplier tubes (PMTs). Its diameter is 13mm with UV glass window (Hamamatsu R4124UV). Each pixel covers $0^\circ.115 \times 0^\circ.115$,, which was expected for the large telescope having a fine imaging pixels from the simulation study [1][19]. Figure 3.3 shows the arrangement of PMTs in the camera, where that of 3.8m telescope is also presented. A field-of-view is $\sim 3^\circ$. At the front of PMTs, the light guide are attached in order to collect photons from the dead spaces between

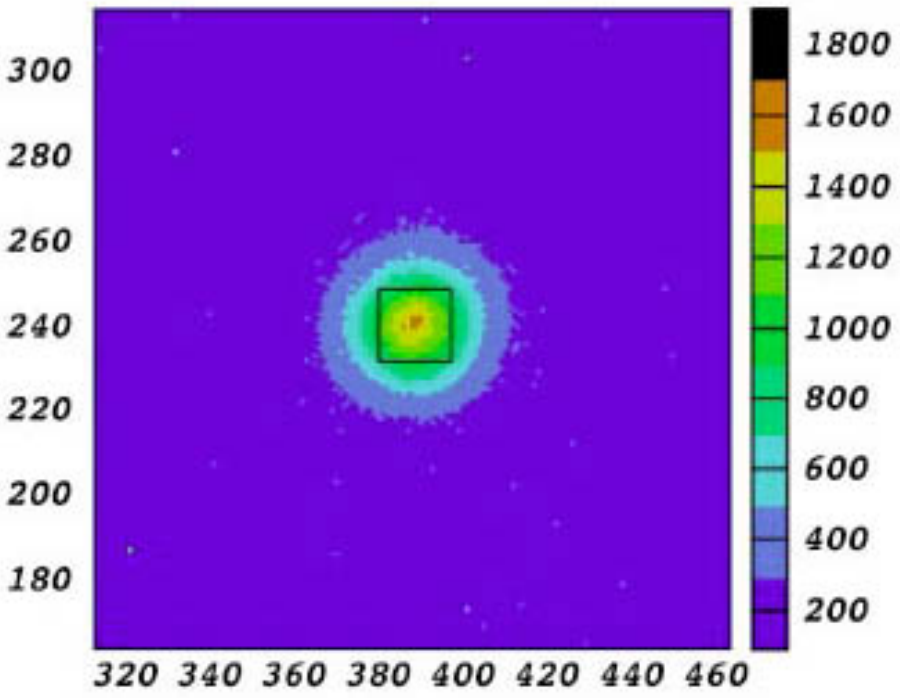

Figure 3.2: CCD image of Sirius on the optic axis. One pixel of the camera (0°.115 square) is superimposed for scaling.

photosensitive area of the PMTs. Groups of 16 PMTs are installed in one amplifier module box. A total of 32 modules are arranged in 6×6 square with the four corner modules missing make up the camera. Each group of PMTs are supplied with same voltage and their gains are adjusted within 15 %.

3.4 Electronics Circuits

The outputs from PMTs are fed to the discriminator and scaler module (DSM), based on the TKO specification, in the electronics hut through 36m twisted cables. In the DSM, the signal from each PMT is amplified, shaped and separated into three signals. One signal is fed to summed output which is a linear sum of 16 input signals ("L-sum"). The signal from L-sum is sent to a CAMAC-based ADC (analogue to digital converter) and to discriminators used for event triggers. Another two signals are fed into two discriminators in DSM: a non-updating discriminator and an updating one. The signal which goes through the non-

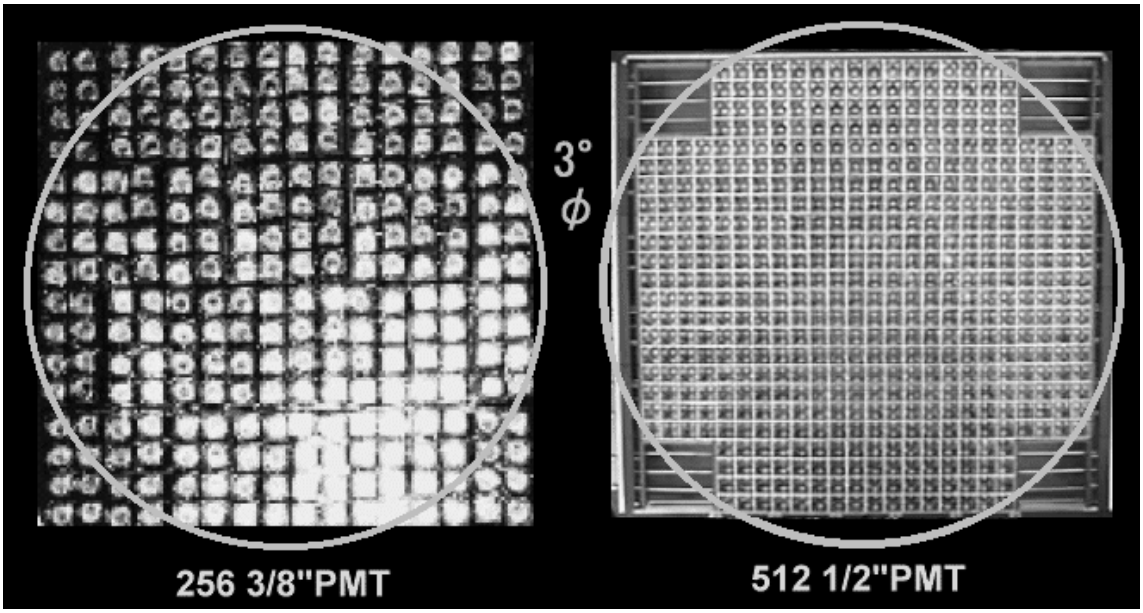

Figure 3.3: Front view of both the cameras of the 3.8m telescope (left) and the new 7m telescope (right).

updating discriminators also separated two signals. The threshold level of the non-updating discriminators are set higher than the updating one. One is used for scaler and the other is fed to summing circuits of which output is proportional to the number of hit channels of innner 16 modules of the camera ("Hitsum") to generate event triggers. The signal going through the updating discriminators are sent to a multi-hit TDC (time to digital converter), both leading and trailing edges of the signal are recorded. Those two timing are measured with 0.5ns resolution, and gives information of the logarithmic pulse height in a way. Figure 3.4 shows an example of the pulse height vs pulse width curve.There are measured in a laboratory with the same electronics and cables using a LED light source. In off-line analysis, the pulse height of each PMT are converted from the recorded timing width using this correction curves. The block diagram is shown in Fig. 3.5.

3.5 Event Trigger and Data Recording

L-sum and Hit-sum from 16 inner PMT modules of the camera are summed in a linear adder module and fed into discriminators. An event is triggered when both of these summed

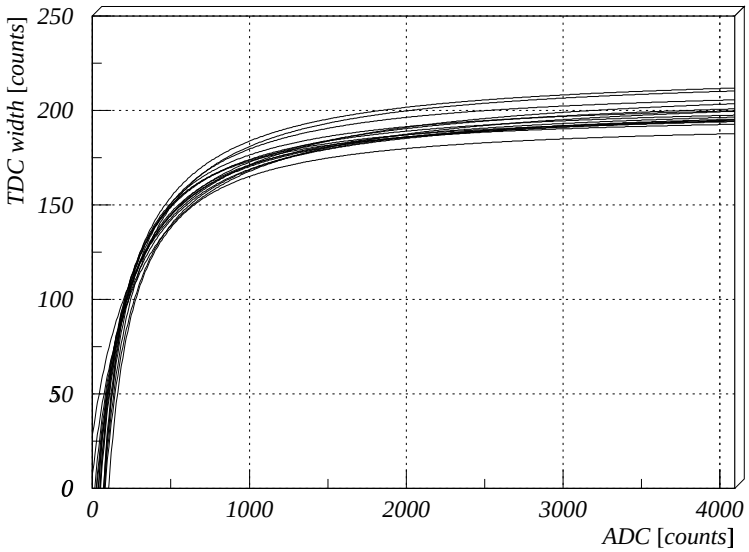

Figure 3.4: Example of the pulse height vs pulse width curve. Sixteen curves from 16 PMTs assmbled in a module. [22]

signals exceed preset values. At present, triggers are generated when there are more than 4 PMTs whose pulse heights are larger than 4 photoelectrons, and inner 16 of 32 PMT module units are concerned with the trigger, which covers a $\sim 1°.8$ diameter of the field of view. In this condition, triggers were generated at $\sim$ 10 Hz [20]. These triggers initiate the data acquisition sequence via an interrupt register module in the VME.

Both charged and timing information from TDCs and ADC of triggered events are sent to a VME-based board computer (FORCE CPU-7V, TurboSPARC 170MHz) through a VME/K-bus interface and a CAMAC crate controller. This computer is operated under the Solaris 2.6 operating system and the UNIDAQ software. The system deadtime is about 15 % and 30 % when the trigger rate is 12Hz and 28Hz, respectively [17]. After observation stopped, the data which is stored in local hard disk is recorded on 4mm DAT for off-line analysis. Typical data size of one event and one day are tens of megabytes and about one of gigabyte of disk storage, respectively.

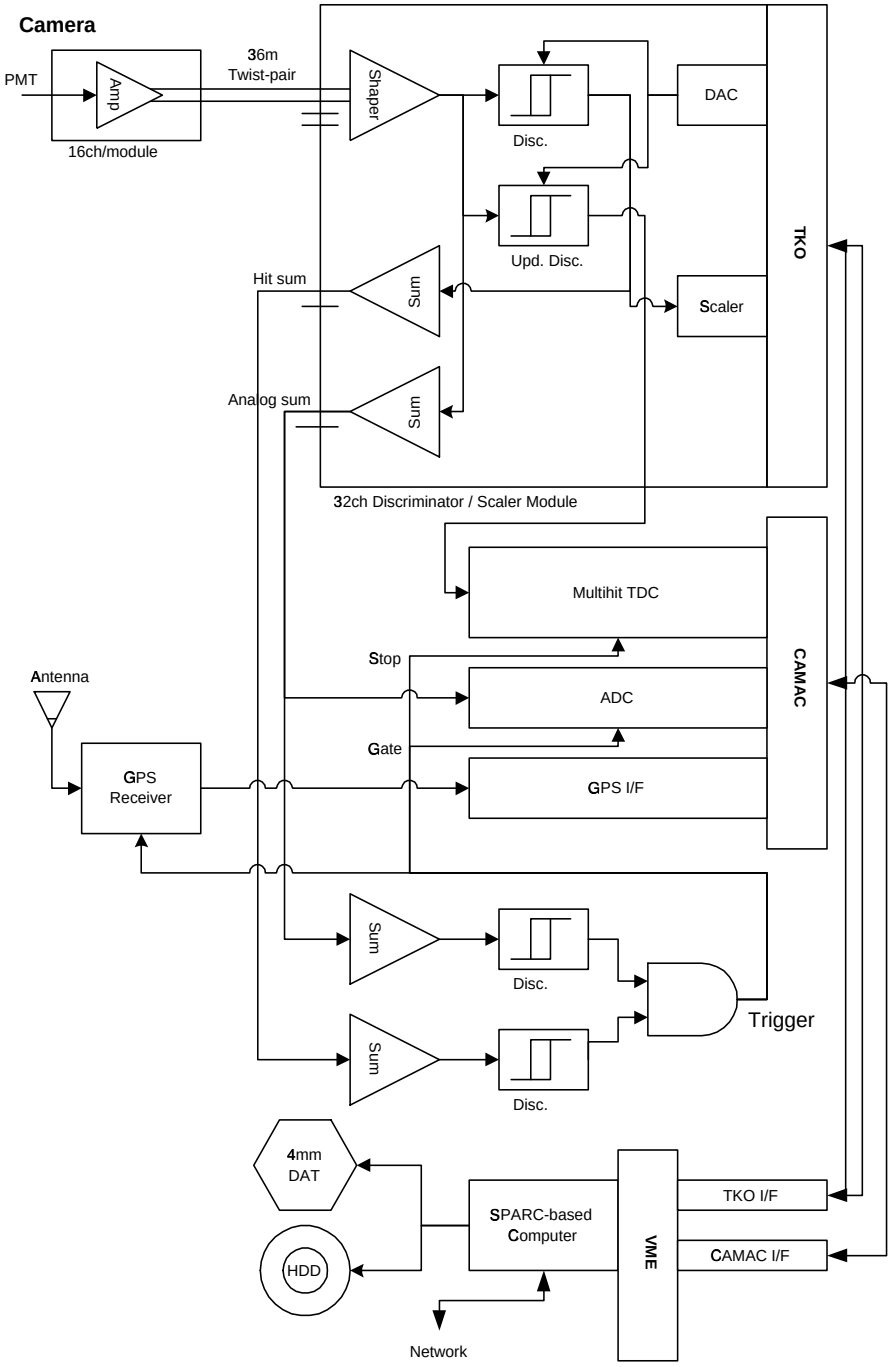

Figure 3.5: Block diagram of electronics [17].

3.6 Telescope Control and Tracking Accuracy

The orientation angle "Alpha" of gamma-ray images is very sensitive to the position of the source in the field of view. Precision of out tracking program were checked when the telescope was first installed. The alt-azimuth mount of the telescope is driven by telescope controller based on a 68K processor board which accepts coordinates of the telescope in azimuth and elevation. The tracking computer calculates the designated coordinates and sends the values via an RS232-C line every 100ms. In parallel, encoder value of the telescope position are received. A real-time Linux (KURT) operating system was adopted as a control software for the telescope to achieve fast response time while retaining full Unix utilities capability. The computer clock is synchronized to UTC by using the NTP software with a GPS receiver (Furuno TS-800) or world-wide time servers through dial-up internet connection in order to maintain tracking accuracy with errors less of than 1 arcmin.

The gamma-ray source candidates are in general not bright at optical wavelengths, and then cannot be directly found its position by checking the counting rates of the PMTs. On the other hand, counting rates of the PMTs increase when the image of bright stars passing through the PMT. When telescope tracks some point of the sky, the field of view rotates. Therefore we can calibrate the tracked point using the enhancement of counting rate of PMTs due to the rotating star in the field of view. The fine pixel of our imaging camera allows the accurate determination of a tracking point as follows.

As mentioned above, the count of the scaler for each PMT give a good indication of the sky brightness in the field of view of the PMT. When bright stars are in the field of view of the camera, the scaler counts of the PMT viewing stars suddenly increase. Such an increase of scaler counts moves from one PMT to the other as the star position rotates as a function of time. The rotation center should be at the center of the field of view of the camera, if tracking of the telescope is correctly done. On the other hand, possible errors of the telescope tracking can be monitored by the change of scaler counts of the PMTs.

3.7 Event Selection Using Timing

The arrival direction of each shower is not determined only from the shower image. However the arrival is determined by combining the image and arrival times of Cherenkov photons contained in the image. In order to use timing information, the accuracy of arrival timing are needed within $\sim$ 1ns. However, the time walk effect of hit pulses come about in discriminator; the timing of the discriminated pulse of photons have offsets depending on its pulse heights. In order to correct this offset, the calibration was done using the LED data. Luminosity of LED are changed by small steps, and transition of arrival timing are recorded in each step. Using this data, the relation of the output of PMT and timing offset are obtained.

We know the relation of the average TDC width of each PMT channel and average ADC of each modules which added 16 PMTs in every luminosity of LED, and following function of TDC are fitted

$$\text{TDC width} \quad = \quad \text{a}\frac{1}{\sqrt{\text{ADC} - \text{pedestal}}} + \text{b}. \tag{3.1}$$

where a and b are arbitrary coefficients determined from the data. Then TDC corrected the time walk effect is

$$\text{TDC width}_{\text{cor}} = \text{TDC} - \text{a}\frac{1}{\sqrt{\text{ADC} - \text{pedestal}}}. \tag{3.2}$$

Timing data of each PMT includes a different offset due to difference of a cable length, a high voltage value, and so on. This offset is estimated using the LED data [23].

In imaging Cherenkov telescopes, stop timing of TDCs are send from the trigger generated also by PMT signals of Cherenkov photons. This scheme is called " self-trigger system", therefore timing of the trigger varies according to the shape of accumulated Cherenkov photons usually fluctuating. In order to correct this fluctuation of the trigger timing, the average timing of hit PMTs in each event is adjusted to the same timing event by event.

After the above timing calibrations, the corrected arrival timing accumulated for all events is shown in Fig.3.6. In case that the correction for the timing calibration is not applied, the

timing is distributed in 26.5ns at full width half maximum (FWHM). After corrected the time walk effect, the timing is corrected within 24ns (FWHM), and after all timing calibrations, the timing almost concentrates within 14ns (FWHM). This distribution of Cherenkov photons are in consistent with that expected from hadron shown simulation.

After timing calibration, the timing distributions and the images of hadron and muon events are shown in Fig. 3.7 and 3.8, respectively. The arrival timing of the muon event concentrated within 10ns (FWHM), on the other hand, that of the hadron event is distributed in 15ns (FWHM), these image shows night sky background distributed uniformly in timing can be clearly rejected [16].

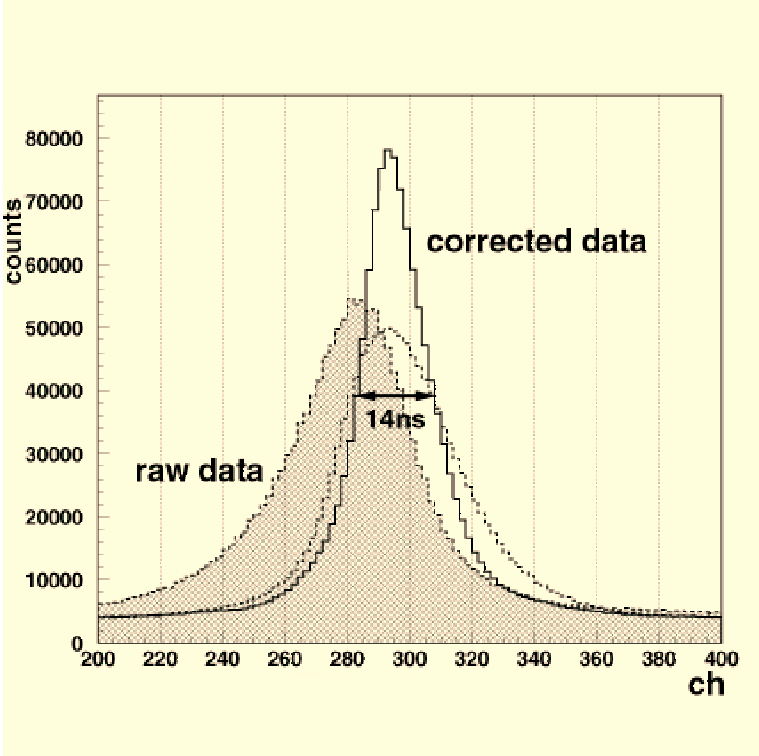

Figure 3.6: Arrival timing of hit PMTs for all events. Used data is off-source for PSR 1706-44. Raw data (hatching), the data after corrected the time walk effect(dashed line), and corrected data after all timing calibrations (solid line) .

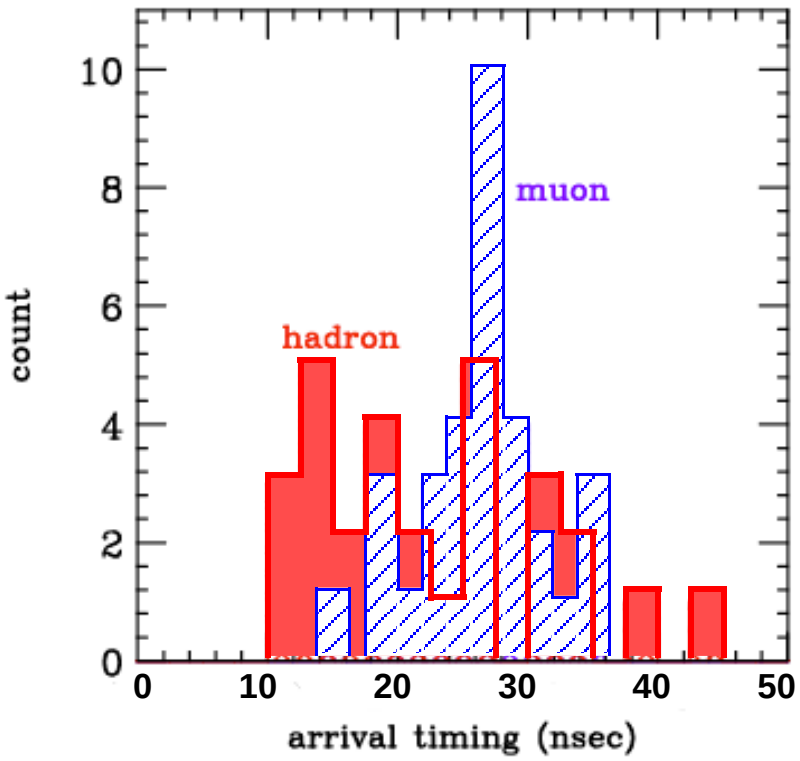

Figure 3.7: Arrival timing of hit PMTs for hadron and muon after removing NSB from timing information.

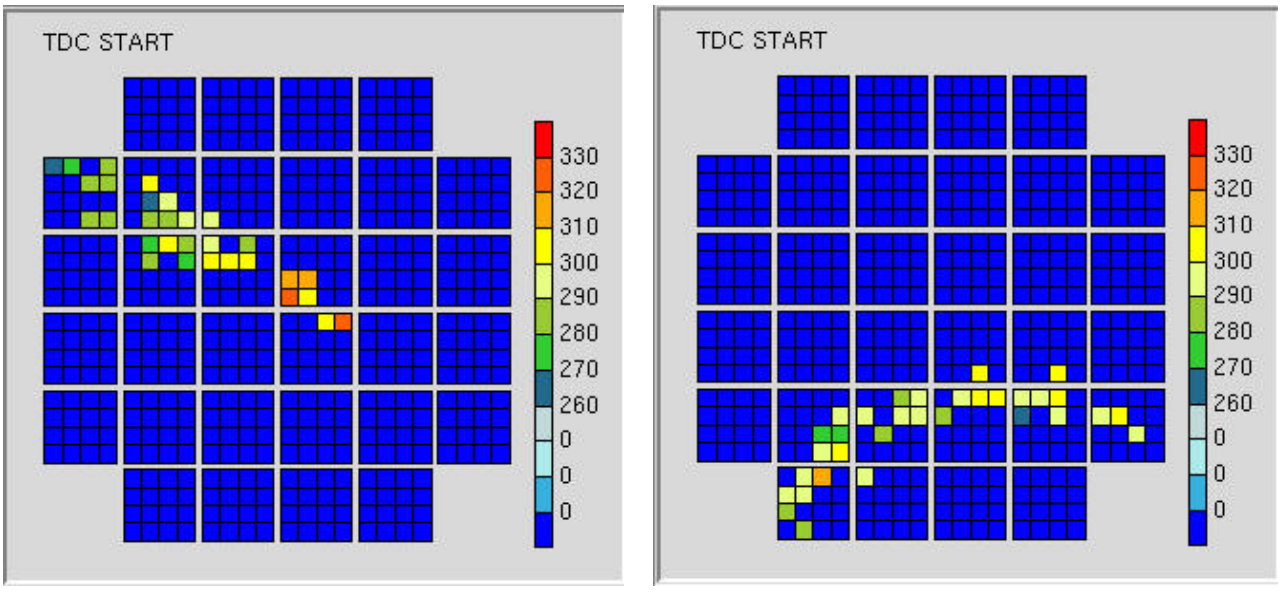

Figure 3.8: Hadron(left) and muon(right) image after removing NSB from timing information

Chapter 4

Energy Threshold

4.1 Night Sky Background Light

The energy thresholds of the 7m telescope for gamma rays and hadrons were estimated using Monte Carlo simulation. In the simulation, the effect of the night sky background (NSB) has to be taken into account. Here we use the following value of the brightness of the night sky which was obtained by averaging the data of Chuveyev (1952) and Babcock and Johnson (1941) summarized in Table 4.1. The mean value from these two groups of results is

$$2.55 \times 10^{-4}\,\mathrm{erg\,cm^{-2}\,sec^{-1}\,str^{-1}}(4300 - 5500\text{Å}). \tag{4.1}$$

This is generally used as the standard intensity of the night sky background light [6]. From PMT's sensitivity, spectral response range of PMT between 300 to 650 nm was used. Assuming that spectral distribution of night sky background light is flat, the number of photoelectrons hitting one PMT per unit time is obtained as follows,

$$\begin{aligned} \frac{dN}{dt} &= \frac{d^3N}{ds\,dt\,d\Omega}\, S_m\, \theta^2\, \epsilon_r\, \epsilon_l \\ &= 1.28 \times 10^{-2}\ \text{photoelectron nsec}^{-1}\ \text{PMT}^{-1}, \end{aligned} \tag{4.2}$$

where S_m is an effective light correcting area, θ is the pixel size of the PMT, ϵ_q is a quantum

Table 4.1: The background light of the night sky [6].

Chuveyev (1952)	Continuous spectrum :	1.5×10^7
	Starlight and zodiacal light :	1.4×10^7
	Total :	2.9×10^7
Babcock and Johnson (1941)	$4000 \sim 4250$ Å :	1.3×10^7
	$4250 \sim 5500$ Å :	2.0×10^7

efficiency of PMTs, ϵ_r is a mirror reflectivity, and ϵ_l is an efficiency of the light guide. The followings are typical values of those parameters :

Spectral response range 350∼600nm ,

Effective light correcting area S_m=$40^2\pi \times 60 = 3.02 \times 10^5$ cm^2 ,

Pixel size θ =0.11 $^\circ$ × 0.11 $^\circ$,

Quantum efficiency of PMT ϵ_q∼0.2 ,

Reflectivity of mirror ϵ_r∼0.75 ,

Light guide efficiency ϵ_l∼0.61 .

Since the output pulse width of PMTs is about 10ns, a number of photoelectrons(p.e) of NSB accidentally hit in this pulse is estimated to N ∼0.128. This value may be fluctuated within about factor 2 by the place, time or weather.

The fluctuation of NSB photons can explain the observed fluctuation of the count rate of PMTs by the Poisson fluctuation. The probability of the fluctuation beyond the hit threshold level is defined.

$$\mathrm{p} \sim \sum_{\mathrm{n=m}}^{\infty} \frac{\mathrm{N^n}}{\mathrm{n!}} \exp(-\mathrm{N}) = 1 - \sum_{\mathrm{n=0}}^{\mathrm{m-1}} \frac{\mathrm{N^n}}{\mathrm{n!}} \exp(-\mathrm{N}), \tag{4.3}$$

where m is the number of photoelectrons which corresponds to the hit threshold level. Expected counting rate are plotted in Fig 4.1.

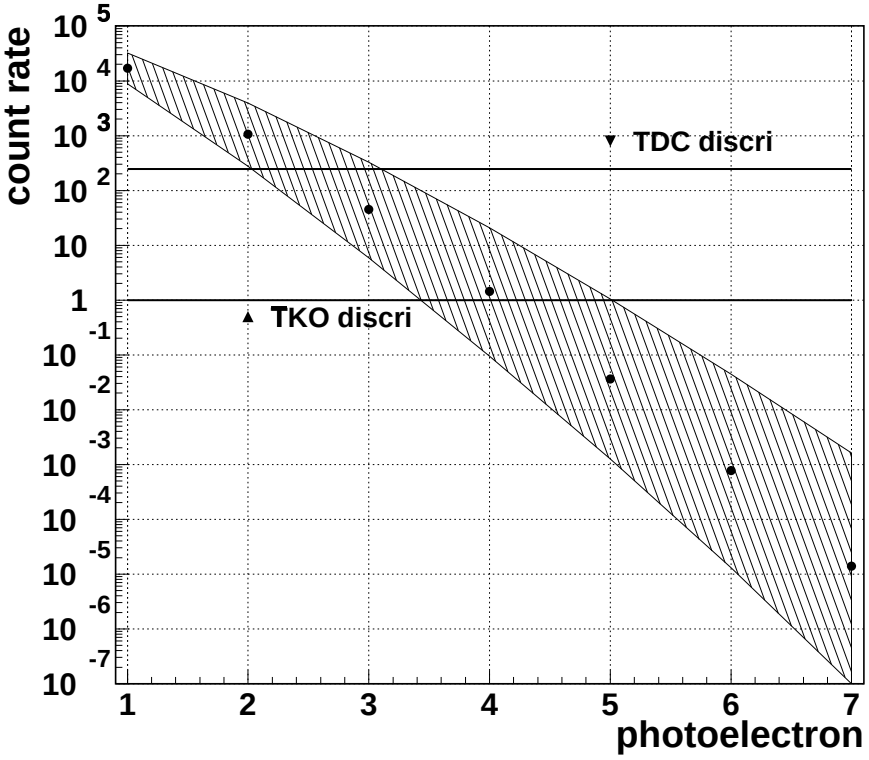

Figure 4.1: The relation of count rate and photoelectrons of hit threshold.

4.2 Hit Threshold Level

The threshold levels of the updating and non-updating discriminators were estimated using the distributions of the timing of pulses recorded by TDC and the counting rate in the scaler, respectively. These distributions are shown in Fig. 4.2 and 4.3. Both plots are measured using the random trigger data obtained by June, 1999. Using these plots, the rate of hit TDC and the average of single count of one PMT per millisecond are estimated

$$\begin{aligned} \text{TDC count rate} &\sim 242 \text{ hits/msec}, \\ \text{TKO count rate} &\sim 1 \text{ hits/msec}. \end{aligned} \tag{4.4}$$

From Fig. 4.1, hit threshold of TDC(updating) discriminator and L-sum(non-updating) discriminator are obtained

Hit threshold level of TDC discriminator $\sim 2.5 \pm 0.5$ p.e,

Hit threshold level of L-sum discriminator $\sim 4 \pm 1$ p.e. (4.5)

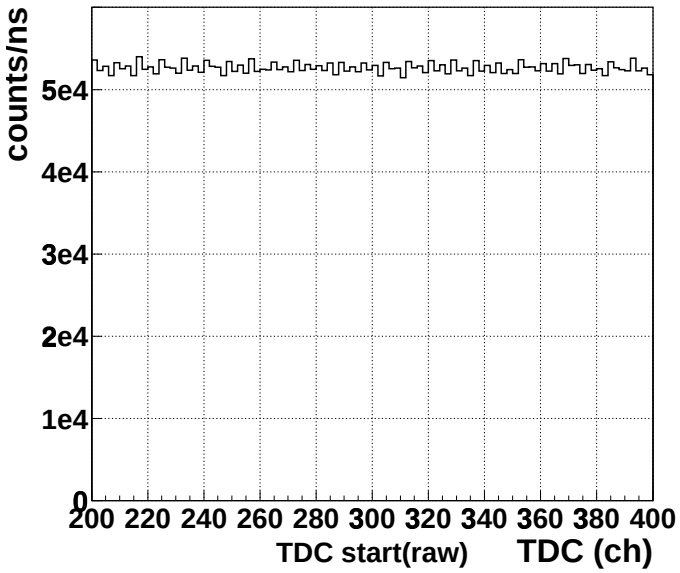

Figure 4.2: Distribution of TDC start(1ch=0.5ns)

4.3 Estimation of Shower Energy

In order to know the energy of a detected shower from the recorded pulse heights of hit PMTs, the conversion ratio of a pulse height to the number of photoelectrons must be obtained at first. Since the sum of photoelectrons (Sumnp) in an event is approximately proportional to the shower energy, we can know the energy of a detected showers. The relation between the sum of TDC width (SumPh) and the shower energy are estimated by comparing the distribution of Sumnp obtained from Off-source data with that of the simulated proton events. In our analysis Sumnp is calculated from the SumPh as mentioned in section 3.4. Figure 4.4 shows the relation of the number of hit PMTs (Nhit) and the SumPh in a

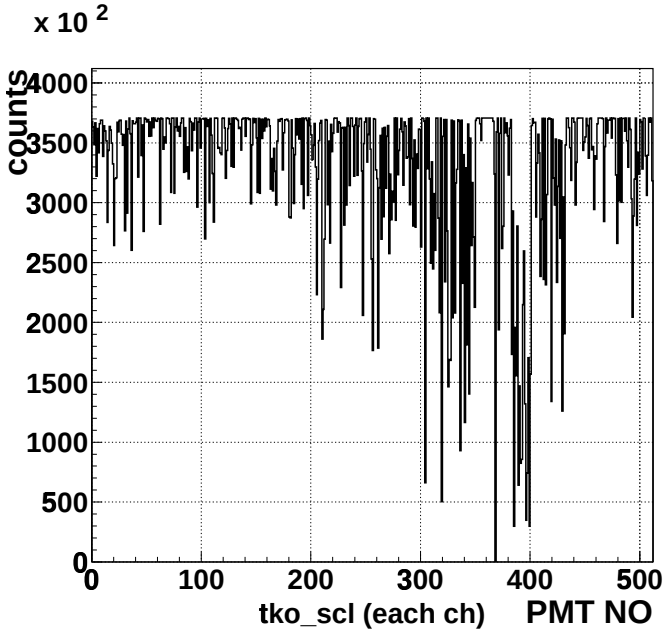

Figure 4.3: Distribution of TKO scaler

Off-source data, and Figure 4.5 shows the relation of Nhit and Sumnp of simulated protons. Simulated condition of proton is as follows: energy region is between 200 GeV $\sim$ 1 TeV, power index is -2.7, and mirror reflectivity is $\sim$ 75 %.

In Fig. 4.6, The ratio of SumPh to Sumnp are affected by the uncertainty of the estimation of the hit threshold level described in previous section. Using its uncertainty of one PMT, the conversion ratio of one photoelectron is estimated to

$$\mathrm{Ph} \sim 14.39 \pm 0.76 \mathrm{ch/1p.e.} \tag{4.6}$$

Figure 4.7 and 4.8 shows the event distributions as a function of the sumPh from observed data which corresponds to the cosmic-ray spectrum and Sumnp of the proton simulation, respectively. Note that both the slopes becomes flatter similarly as energy decreases. It is likely due to the decrease of the detection efficiency at the trigger threshold level. By comparing the shape of observed spectrum with the simulated spectrum around the bending region of $\sim$ 600GeV, hit threshold level can be estimated besides the use of the single count rate in previous section, As the results, the hit threshold level of Off-source data and proton

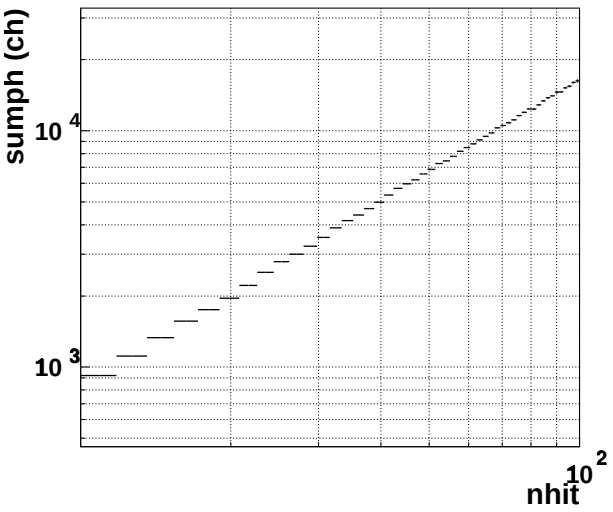

Figure 4.4: The relation of the Nhit and the SumPh (ch) in an Off-source data.

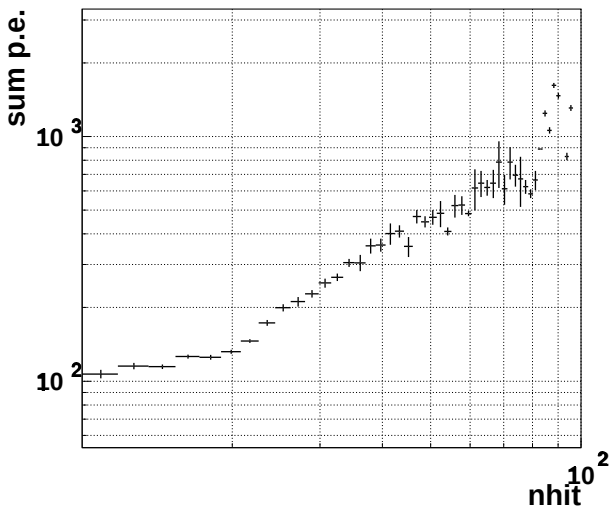

Figure 4.5: The relation of the Nhit and the Sumnp in a proton simulation.

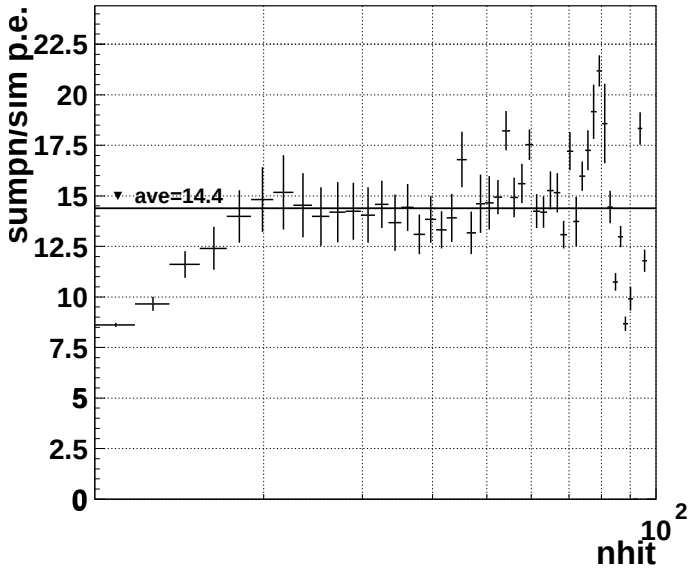

Figure 4.6: The ratio of Ph to photoelectron

simulation are $\sim$ 500$\sim$700 ch and $\sim$ 30$\sim$40 p.e, respectively. Then, Ph $\sim$ 15ch/p.e. is obtained. This result is well consistent with the result of conversion of pulse height into photoelectron.

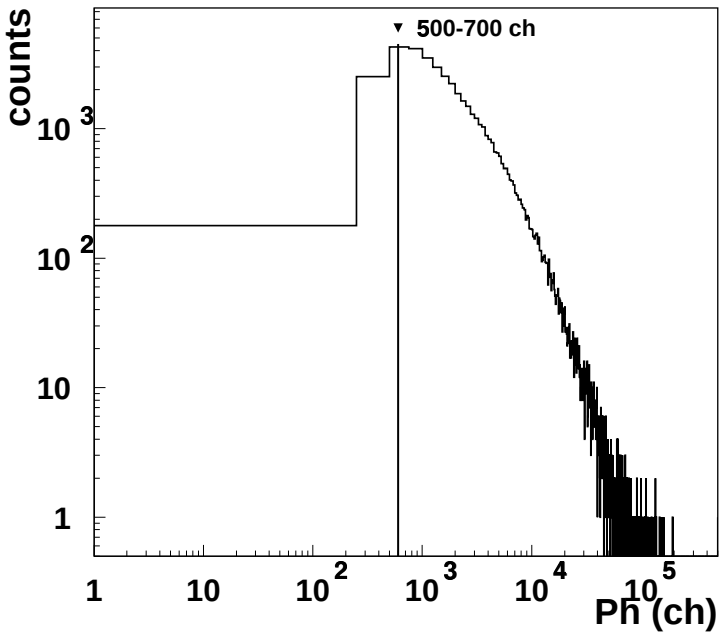

Figure 4.7: The spectrum of cosmic-ray (Off-source data)

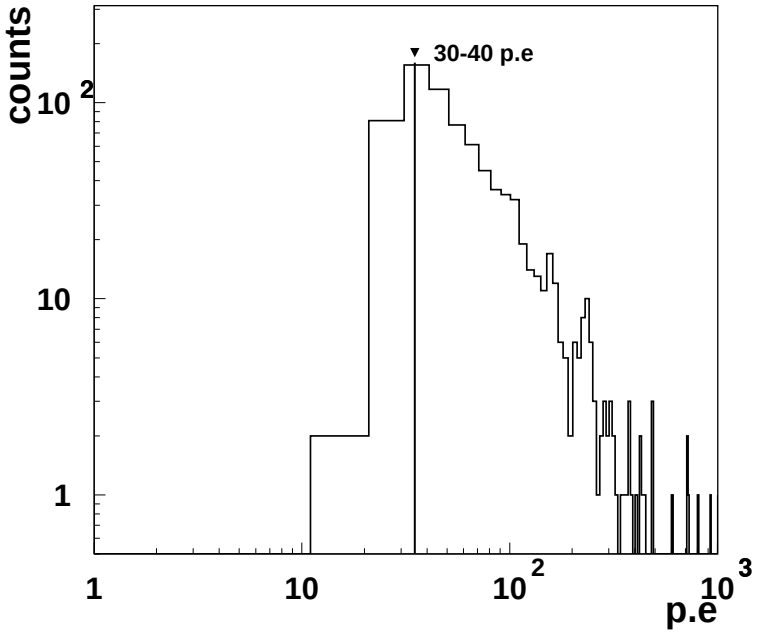

Figure 4.8: The spectrum of protons (Simulation)

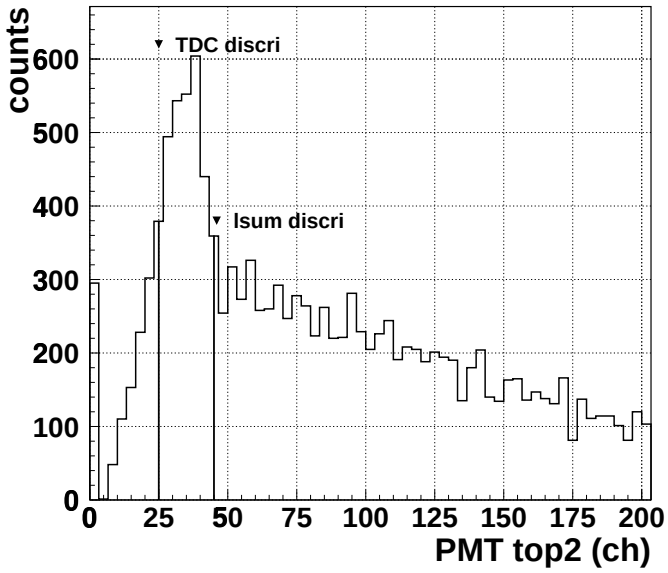

Figure 4.9: Spectrum of the night sky background light

The hit threshold level for update and non-update discriminators were also estimated using the Off-source events of which Nhits are less than 5 since such events are considered to generate by accidental coincidence between NSB and small hadron shower. Figure 4.9 shows pulse height distribution of PMTs having two largest signals on one event, Since largest two PMT signals are considered to NSBs or hadrons in such events, this distribution is overlapped the spectrum of NSB and hadrons. In Fig.4.9, the peak in low channel region is due to the NSB and flatter larger one is due to hadron showers. From equation(4.4), the counting rates of TDC(up-dating) and L-sum(non-updating) discriminators are about 242 hits/msec and 1 hit/msec, which indicates that the rise point around 50 counts corresponds to the threshold level of L-sum and the half point around 25 counts in the peak correspond to TDC discriminator.

Using Equation (4.6), hit threshold level is represented as a function of photoelectron from above values.

$$\text{Hit threshold level of TDC discriminator} \sim 2\text{p.e.},$$

Hit threshold level of L-sum discriminator $\sim$ 3 p.e.. (4.7)

These results are also consistent with the results using count rate of NSB.

4.4 Energy Threshold

The relation of the energy threshold and photoelectron is obtained using a Monte Carlo simulation. Figure 4.10 and 4.11 show the number of average photoelectron per each energy for gamma rays and hadron showers, respectively. Parameter values used here are described in previous section, and simulated energy regions of proton is 200GeV $\sim$ 6TeV with the primary differential power of -2.7 and gamma ray is 100GeV $\sim$ 1TeV with the primary differential power of -2.5. Triggers are generated when there are more than 4 PMTs of which pulse heights are larger than 3 photoelectrons.

Using Fig. 4.8, hit threshold level is estimated $\sim$ 40p.e., energy threshold for proton are obtained $\sim$ 800GeV from Fig.4.10. Since the number of particles in a hadron shower is roughly one third of those of gamma-ray showers, the energy threshold for gamma ray are estimated 200 $\sim$ 300 GeV.

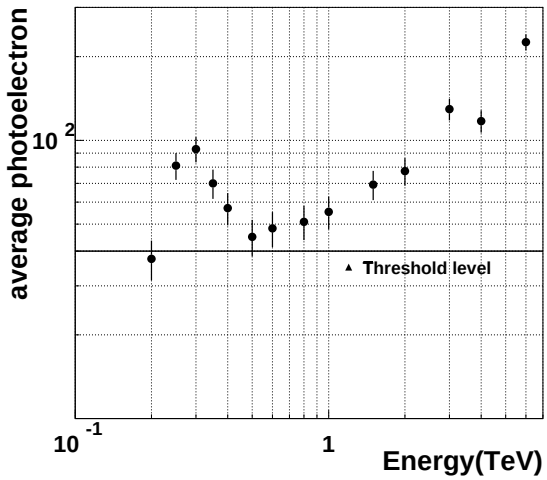

Figure 4.10: The relation of energy and p.e. (Proton simulation)

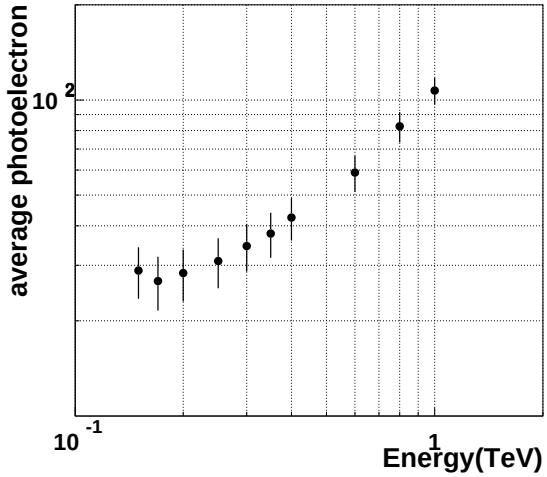

Figure 4.11: The relation of gamma-ray energy and p.e. (Gamma-ray simulation)

4.5 Mirror Reflectivity and Light Guide Efficiency

In order to check the variation of the reflectivity of mirrors, the trigger rate for hadron showers was examined in every month as shown in Fig. 4.12. To remove the effect of NSB, Nhits $\geq$ 5 was required. Considering of the weather and humidity, Off-source data, with good condition were used. This figure shows that trigger rate was constant, which of means that the reflectivity of mirrors are also constant. Actually, the reflectivity measured in June was $\sim$ 75 %, and in November is $\sim$ 70 %. Therefore, the reflectivity looks almost constant.

Figure 4.12 also includes the trigger rate of which data was observed without the light guide. this rate was almost half of those with the light guide. The light guide was designed for gathering double light in effective area of PMTs. Thus the light guide efficiency is estimated $\sim$ 61 %, where the photocathode of PMT covers only $\sim$ 35% of the area of one pixel. When count rate of the threshold was half, the number of photon are found to twice (See Fig. 4.7), which corresponds to the efficiency of $\sim$ 61 %.

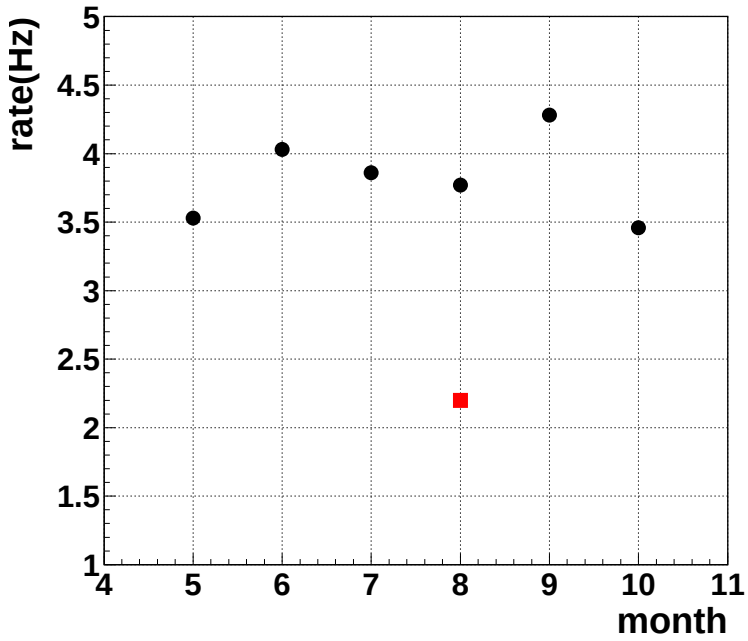

Figure 4.12: The variation of the trigger rate for each month (1999). The square mark shows the trigger rate of which data was observed without light guide.

Therefore, The reflectivity of mirror is $\sim$ 75 %, and the light guide efficiency is obtained to be $\sim$ 61 %.

4.6 Summary

In summary, energy thresholds and significant parameters are described as follows

Energy threshold of proton $E_p < 700 \sim 800$ GeV (power index -2.7),

Energy threshold of gamma ray $E_\gamma \sim 200 \sim 300$ GeV (power index -2.5),

TDC discriminator hit threshold level $\sim 2.5 \pm 0.5$ p.e.,

L-sum discriminator hit threshold level $\sim 4 \pm 1$ p.e.,

Ph/p.e $\sim$ 15ch/p.e.,

Reflectivity of mirror $\sim$ 75 %,

Light guide efficiency $\sim$ 61 %,

Chapter 5

Analysis

5.1 Crab Nebula

The Crab is the standard candle of TeV gamma-ray emission and a typical pulsar which is youngest and has pulse period of 33.2ms (See Fig 5.1). Pulsed radiation of the Crab pulsar was observed in multi-band from radio to gamma ray, which well understood as an synchrotron emission from high energy electrons accelerated up to $\sim$ 100 TeV in the nebula. The higher energy component above $\sim$ 1 GeV is considered to be produced by the Inverse Compton scattering between these very high energy electrons and synchrotron photons emitted by itself (Self-Compton Model) and ambient photons in the nebula.

Our group has observed gamma ray above 4 TeV from the Crab nebula at the large zenith angles, using 3.8m telescope during 5 years.

Since the Crab Nebula is the most reliable gamma-ray source, it is useful to observe the Crab nebula with 7m telescope for examining its performance.

5.2 Large Zenith Angle

Since the Crab is placed in northern hemisphere, it was observed in the large zenith angles in Woomera. When the zenith angle is larger, the atmosphere becomes thick. Therefore, the height of maximum developing point of a shower is higher and the length between a

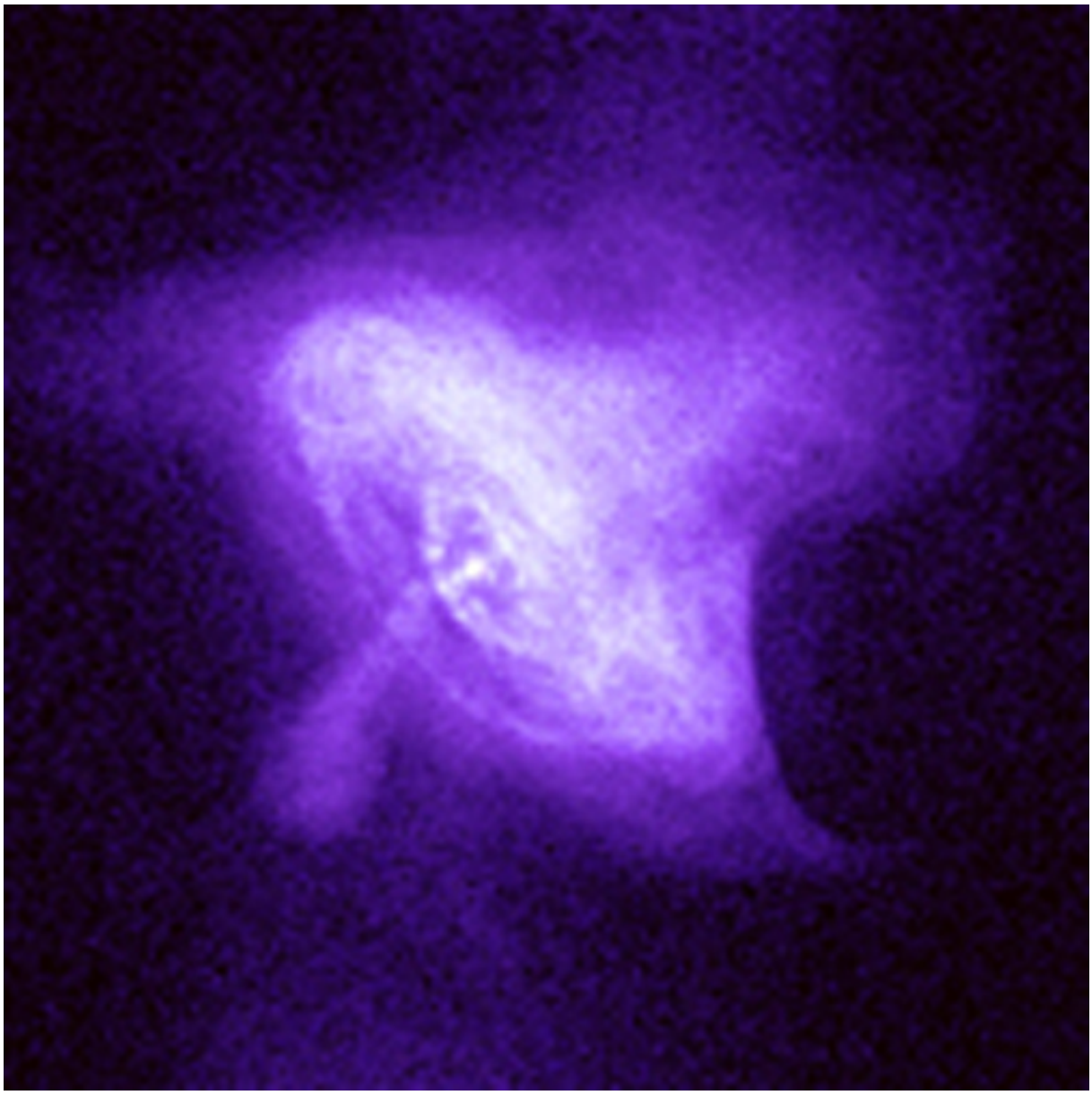

Figure 5.1: An X-ray image of the Crab Nebula taken by Chandra X-ray satellite. The bright central X-ray source is the Crab pulsar.

shower and a telescope is longer. Then energy threshold becomes higher, while effective area increases inversely [9]. Hence we can observe the gamma rays from the Crab at energies approximately 1.5TeV using 7m telescope.

The height dependence of the atmospheric density is usually represented,

$$\rho(h) = \rho_0 \cdot \exp(-\frac{h}{H}), \tag{5.1}$$

$$H = 7.1\text{km}. \tag{5.2}$$

where h is a height above the ground level and ρ_0 is an atmospheric density on the ground-level. When high energy particles come into the atmosphere at zenith angle of θ, the amount of matter along that path x_θ is written as,

$$x_\theta = \frac{\rho_0 \cdot H \cdot \exp(-\frac{h}{H})}{\cos\theta}. \tag{5.3}$$

Thus, the passed height is

$$h_\theta = h_0 - H \cdot \ln(\cos\theta), \tag{5.4}$$

where h_θ is the height at the zenith angle of 0°, and also the change of the refraction index can be written as

$$n(h) = 1 + a\rho(h) = 1 + a\rho_0 \exp(-\frac{h}{2H}). \tag{5.5}$$

When the height is h_θ, the angle between a running particle and emitted Cherenkov lights becomes

$$\alpha_\theta = \sqrt{2a\rho_0 \cos\theta} \cdot \exp(-\frac{h}{2H}) = \alpha_0\sqrt{\cos\theta}, \tag{5.6}$$

where α_0 is a Cherenkov angle at the height of h_0.

Therefore, the radius of Cherenkov ring on the ground is as follows

$$r_\theta = \frac{h_\theta}{\cos\theta} \times \alpha_\theta = \frac{[\alpha_0(h - H\ln(\cos\theta))]}{\sqrt{\cos\theta}}. \tag{5.7}$$

The radius of Cherenkov ring increases from r to r_θ. The effective area at zenith angle of 53° is about 4 times larger than that at zenith angle of 0°.

In the large zenith angle method, the size of image parameter varied. These image parameters in general shrinks as,

$$\text{width, length} \propto \alpha_\theta \propto \sqrt{\cos\theta}, \tag{5.8}$$

due to the increase of the distance between a telescope and a shower. This shrink of the image parameter makes it difficult to distinguish images between gamma ray and cosmic ray.

Schematic diagram of the principle of the large zenith angle observation is shown in Fig.5.2.

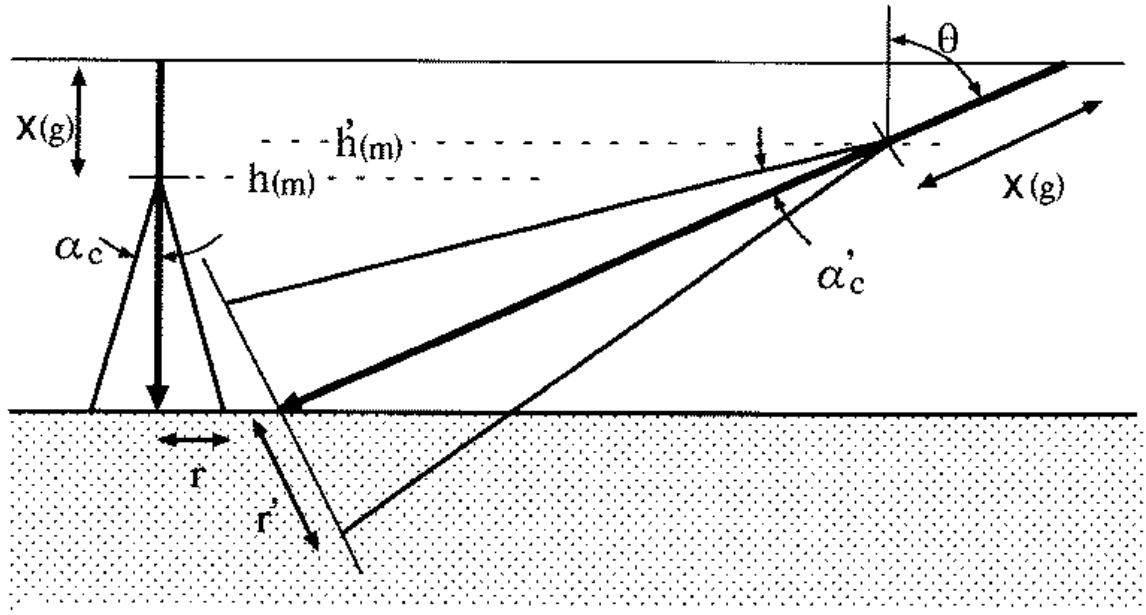

Figure 5.2: Schematic diagram of the principle of the large zenith angle observation.

5.3 Observation of the Crab Nebula

The Crab nebula has been observed with the CANGAROO 7m telescope for two months. Observation time summarized in Table 5.1. We have observed the Crab region near its culmination at zenith angle 53°. We take each on/off source run. In the on/off tracking method, the Off-source observation with no prior gamma-ray source in the field of view is done night by night under the almost same conditions as the On-source observation except the bias of a few degree at Right Ascension. The Off-source data are used to estimate the background counts in the imaging technique. Calibration runs are done in every observation to measure the relative gain of PMTs if by using the 20ns wide light pulse emitted from a blue LED locating at the center of the reflector.

Usually, telescope tracks the target object on the center of field of view for On-source.

However, in this observation, the Crab was shifted from the camera center by 0.4 degrees. Since bright stars exist near to the Crab nebula, especially $\zeta-$Tau which is placed 1°.1 apart from the Crab and its magnitude $\sim$ 3.0. Those bright stars are worried to increase the trigger rate dramatically, and then we have to move those bright stars out of the field of the view of the camera.

Offsets for the distance between the Crab nebula and the camera center is shown in Table.5.2, and the position of the Crab and near stars in the camera are shown in Fig. 5.3.

Table 5.1: Summary of observations of the Crab nebula with the 7m telescope

Month		Raw		Selected	
		hours	events	hours	events
1999 Dec	On-source	22.6	1027557	− − −	− − −
	Off-source	16.0	502915	− − −	− − −
2000 Jan	On-source	29.8	715064	10.2	144864
	Off-source	29.1	875466	9.3	141252
Total	On-source	52.4	1742621	10.2	144864
	Off-source	45.1	1378381	9.3	141252

Table 5.2: Offsets for distance between the Crab nebula and camera center.

	the Crab position	Offset (11/30 $\sim$ 12/9)	Offset (12/9 $\sim$)
Right Ascension	83°.63288	-0°.54	-0°.25
Declination	22°.01446	0°.50	0°.58

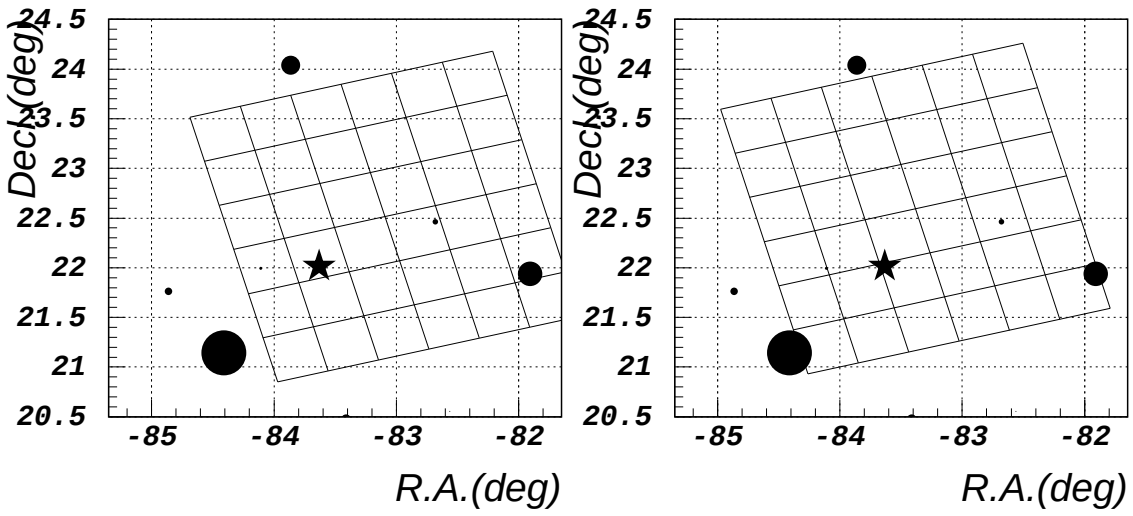

Figure 5.3: The relation of the Crab and camera position. The star mark is the Crab position.Lower left large circle is the position of $\zeta-$Tau, and the square is camera frame. The left figure is the position during 11/30 to 12/9. The right figure is the position from 12/9.

5.4 Noise Reduction

At the first stage of the analysis, to examine the conditions of the observations, rough selections of requiring the minimum number of hit PMTs are applied to all of the data, taking into account followings: the sky and air conditions, the horizontal coordinates, and transient electronic noises.

Since only a small part of the PMTs contain Cherenkov lights from a shower, and almost PMTs include only night sky background photons, NSBs deform imaging parameters. Therefore, cluster cut is applied to remove PMTs hit by night sky background or electronic noise remaining after above selections. If a hit pixel has no adjacent hit pixel in its 8 neighbor pixels, this hit pixel is classified to an isolated PMT and regarded as a accidental hit by NSB, as shown in Fig. 5.4.

After the cluster cut, the timing calibration is applied for correcting variation of PMT

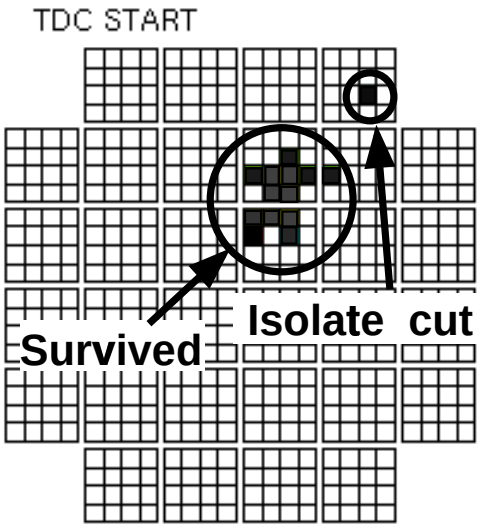

Figure 5.4: Typical isolated PMT. Such isolated PMT was omitted from analysis in cluster cut.

and modules. As the timing calibration, each event is corrected for the time jitter using LED data, and then the average value of arrival timing distribution of each events are aligned. The detail was described in Section 3.7. The arrival timing accumulated for all events of Off-source data of the Crab is shown in Fig. 5.5. In case that the correction for the timing calibration is not applied, the timing is distributed within 25ns. After the calibration, the timing almost concentrates within 14ns.

Sometimes high gain PMTs were found in the single count rate of event monitor. These PMTs affect the imaging analysis, therefore, they are rejected. Figure 5.6 shows the distribution of the centroid of images of Off-source in the field of view of the camera. Figure 5.6 also shows the centroid of images in the region $x \leq -0.5$ and $y \leq -0.5$. then this region was rejected in this analysis.

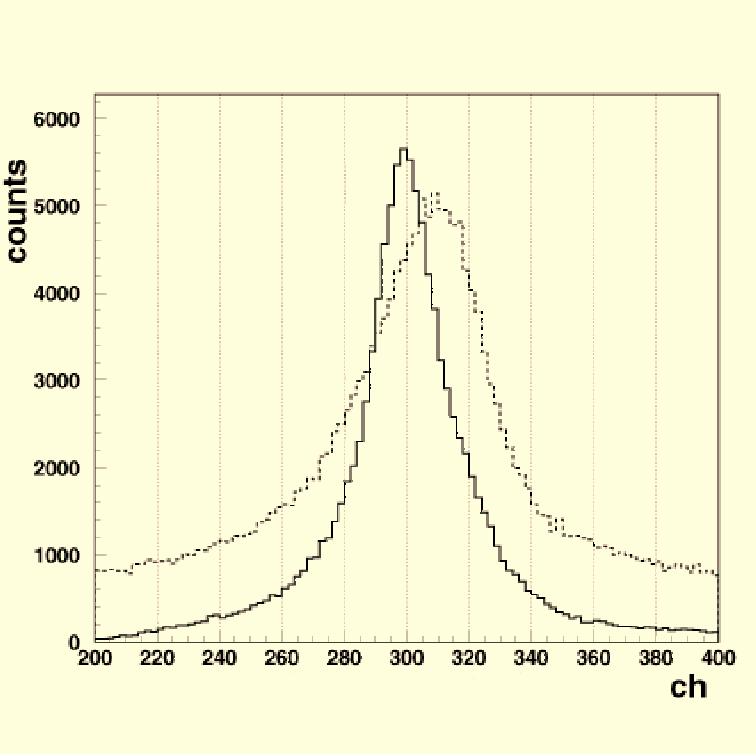

Figure 5.5: The arrival timing of hit PMTs for all events of the Crab Nebula. Row data (dashed line) and Corrected data (solid line).

5.5 Selection of Gamma-ray like Images

An image of the event selected by the previous cuts was fitted using an elliptical shape. The image parameters defined in the section 2.3 were calculated for each event. First, the parameter distributions and the two-dimensional correlation between two parameters calculated by the Monte Carlo simulations for gamma ray or proton induced shower are shown in Fig.5.7 and 5.8. Based on these results, selection criteria for the enhancement of a gamma-ray signal are defined as follows:

$$0^\circ.45 \leq \text{Distance} \leq 1^\circ.1 \tag{5.9}$$

$$0^\circ.03 \leq \text{Width} \leq 0^\circ.12 \tag{5.10}$$

$$0^\circ.05 \leq \text{Length} \leq 0^\circ.4 \tag{5.11}$$

$$0.43 \leq \text{Concentration} \leq 0.9 \tag{5.12}$$

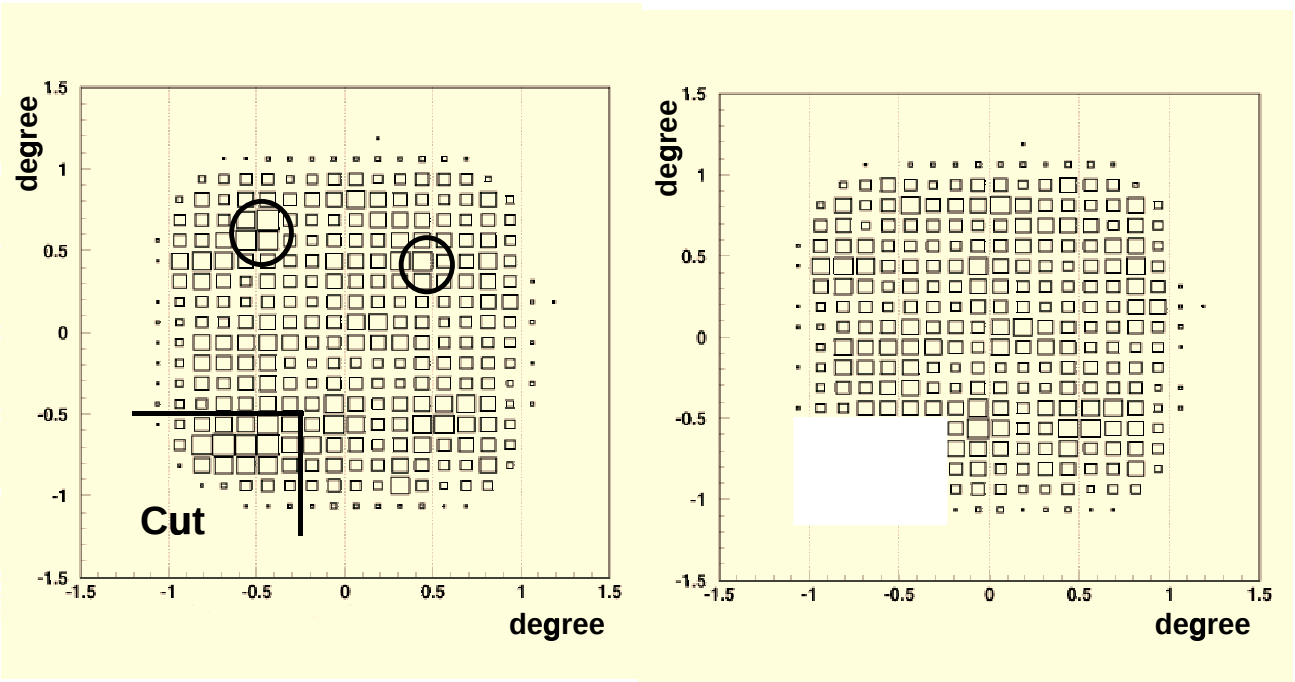

Figure 5.6: Image centroid distributions of Off-source in Jan. 2000, before the omitting high gain PMTs (left) and after (right).

$$\text{Distance} \geq \text{Length} \tag{5.13}$$

To reject noise events which passed through above cut, we applied simple cuts requiring minimum number of hit PMTs to be 5 PMTs, and minimum total pulse height of TDC counts of hit PMTs (Phsum) to be 500 counts, respectively. Since such events are considered to generate by accidental coincidence between NSB and small hadron shower of which is less than the energy threshold. We also set 50 hit PMTs for the upper limit, for the energy of Cherenkov light from hadron showers are larger than that from gamma rays. Figure 5.9 shows the number of hit PMTs for the Crab Nebula Off-source, and Figure 5.10 shows the number of hit PMTs for gamma-ray and proton simulations of the Crab nebula. By applying both this lower and upper cut for the number of hit PMTs, the backgrounds can be further reduced. Even after those reductions, some concentrations of the events in field of view still remains. These concentration looks made by noisy PMTs of which maximum total pulse height of TDC counts (Phsum) exceed 3500/ns, then images containing such PMTs were removed. then these centroid images were rejected.

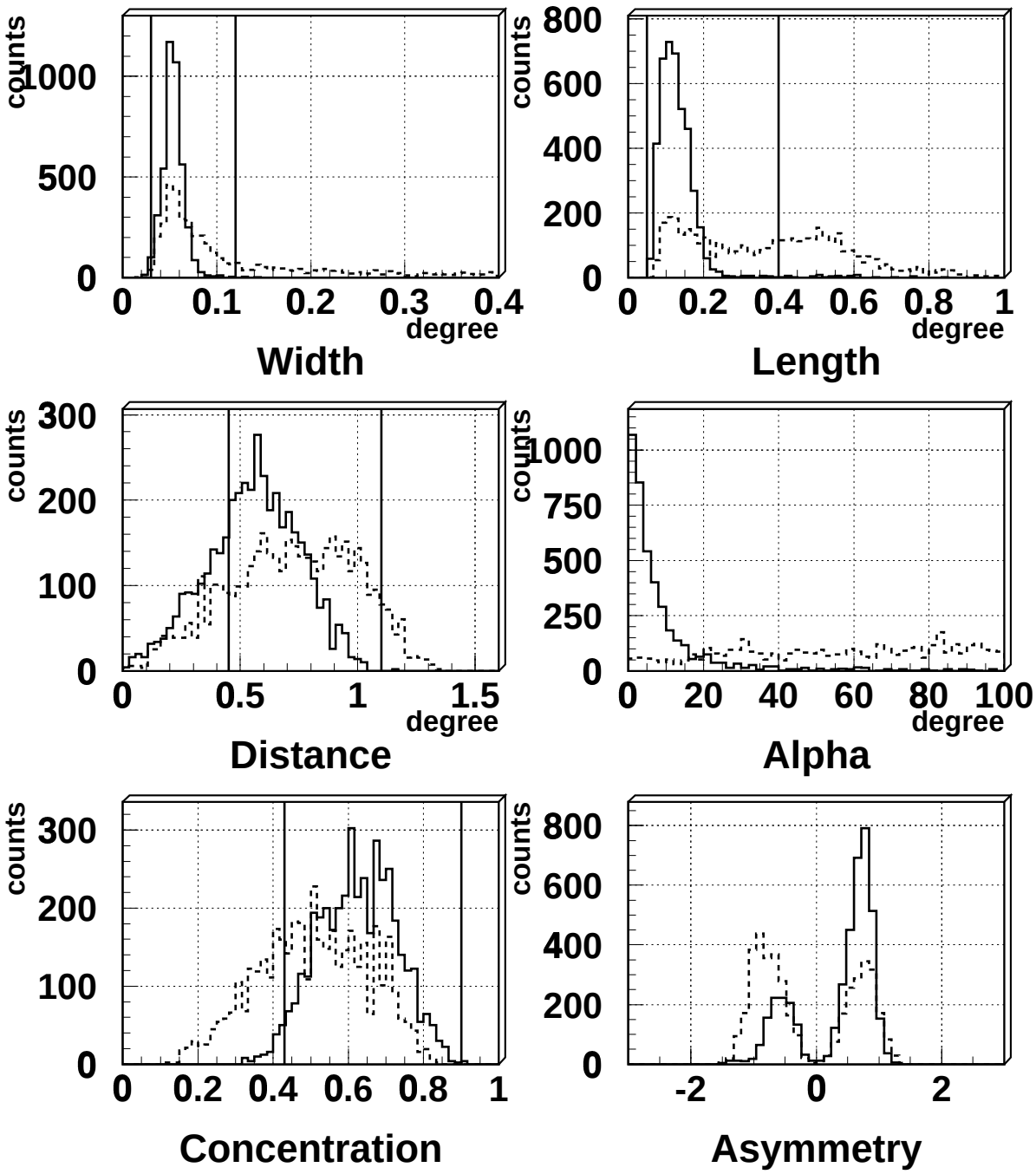

Figure 5.7: Each image parameter calculated by Monte Carlo simulation for the Crab Nebula. Solid line is for a shower due to gamma ray and dashed line is for a shower due to proton. Selection criteria of each parameter are shown drawing line.

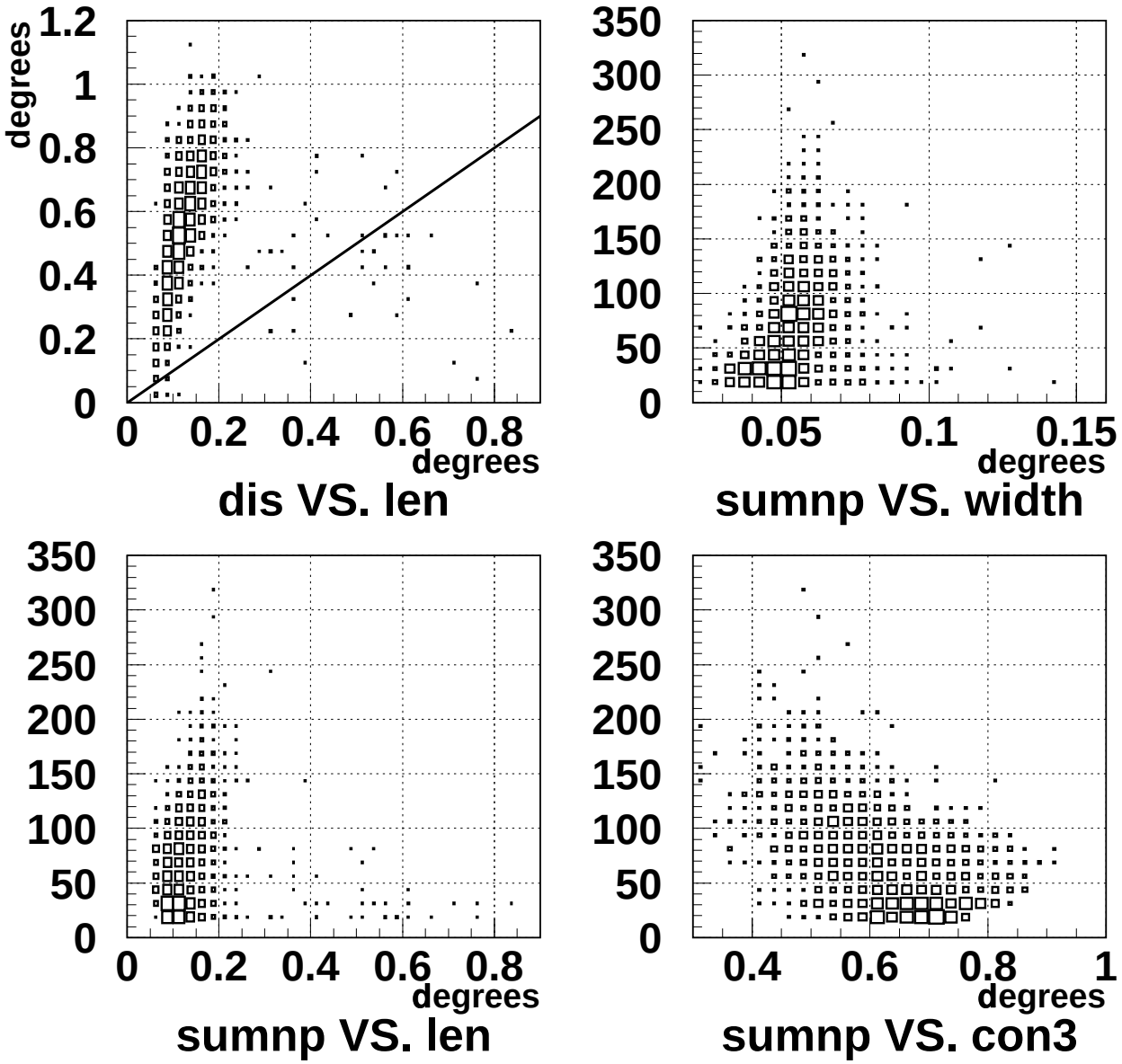

Figure 5.8: The scatter plots of image parameters and the numbers of sum of photoelectrons(Sumnp) for gamma rays. Selection criteria of each parameter are shown as a drawing line.

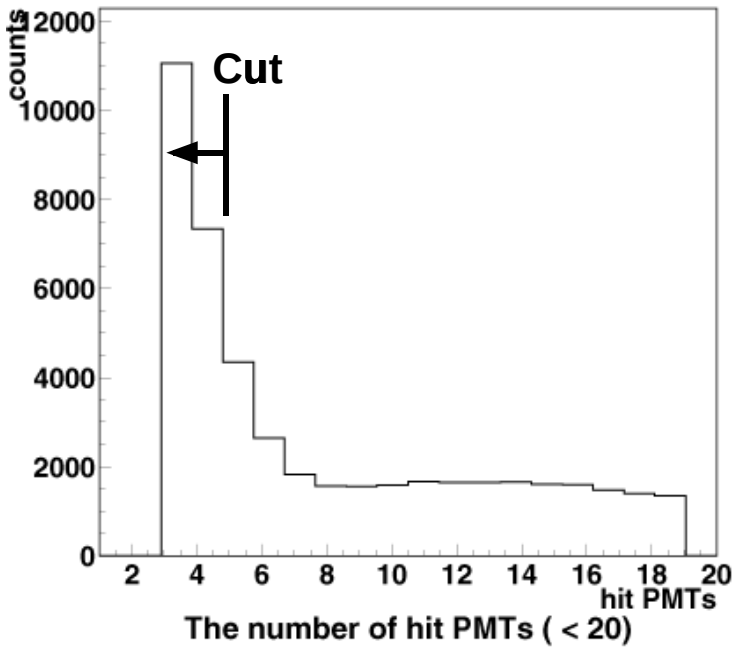

Figure 5.9: Distribution of the number of hit PMTs (Nhit) for the Crab Off-source. (Nhit $\leq$ 20) Nhits which are less than 5 are considered to generate by the accidental coincidence.

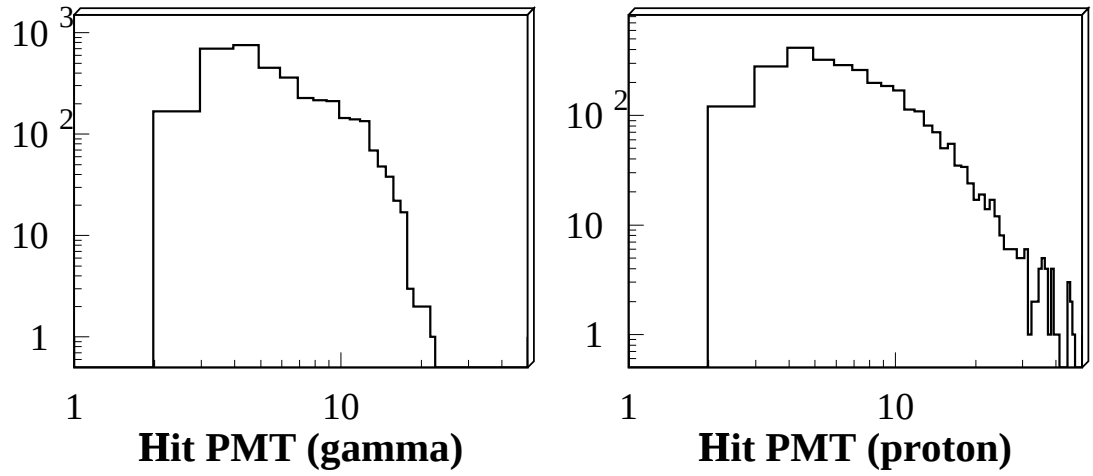

Figure 5.10: Distribution of the number of hit PMTs (Nhit) for simulated gamma rays and protons for the Crab nebula. Nhit of gamma rays are less than 30.

5.6 Results

The variation of the alpha distribution according to these selections is seen in Fig. 5.11. The data of 10 hours observation in January 2000 was used here. After applying the distance cut, a peak of alpha distribution appear near 0°, then, this peak is gradually enhanced by following image parameter cuts, Width, Length, and Concentration. For the events passing through these cuts, gamma-ray signals from the Crab appear as a positive excess around 0° in the alpha distribution of the On-source events against the Off-source events. However, its statistics is not significant yet.

Figure 5.12 and 5.13 shows the detection effective area and the spectrum for protons and gamma rays for the Crab at the large zenith angle using the simulation. From these figures, we find the threshold energy for gamma rays for the Crab at the large zenith angle is ~ 1.5 TeV, and the effective area is $\sim 3.04 \times 10^4 \mathrm{m}^2$.

According to the report of Whipple group [5], Integral flux above 1 TeV is

$$\mathrm{I}\ (\geq 1\mathrm{TeV}) = (2.1 \pm 0.2 \pm 0.3) \times 10^{-7} \mathrm{m}^{-2} \mathrm{s}^{-1} \tag{5.14}$$

Therefore, expected number of Cherenkov photons are $\sim 200/10$ hours.

Still our analysis for the Crab is on going. As the orientation of gamma-ray images is very sensitive to the position of the source, target position in field of view is checked using the starlight signals from scaler count, and all observed data of 40 hours will be investigated. After analyzing all observed data, expected number of Cherenkov photons are $\sim 800/40$ hours and more clearly result will be obtained.

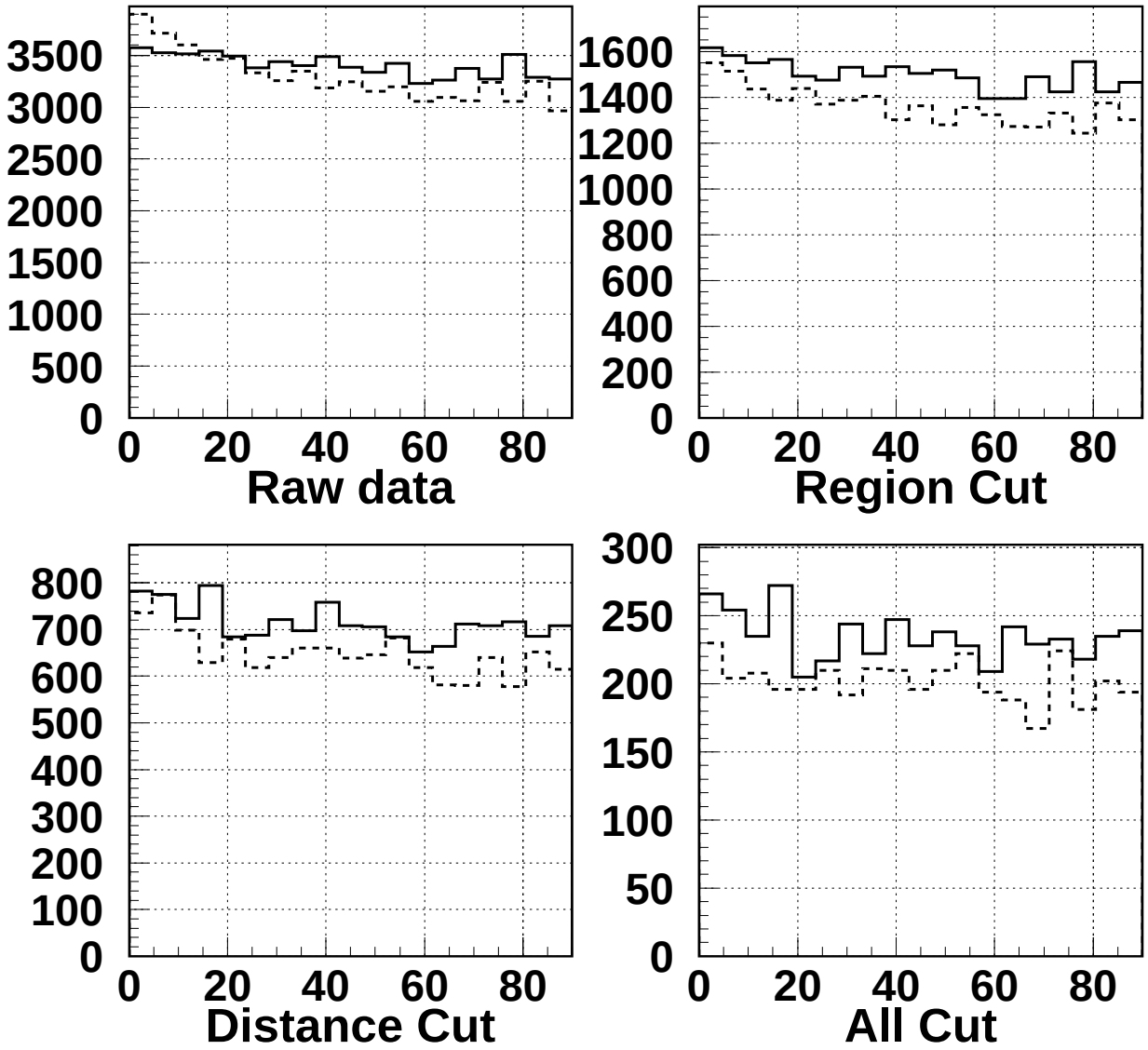

Figure 5.11: Variation of Alpha distribution with shape parameter cut using data sets from Jan 2000.

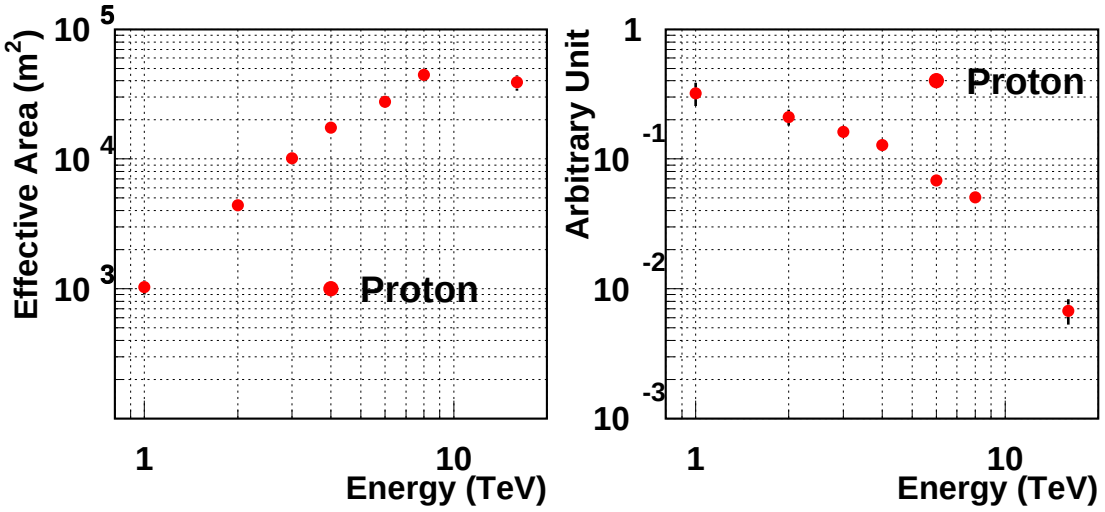

Figure 5.12: Simulated effective area (left) and spectrum(right) for protons for the Crab at the large zenith angle. Differential power index is -2.7.

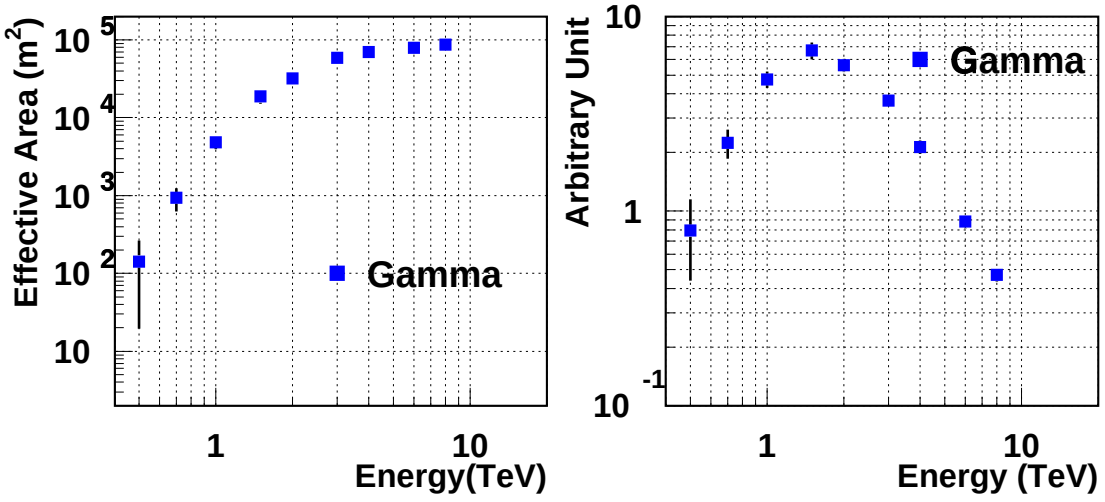

Figure 5.13: Simulated effective area (left) and spectrum(right) for gamma rays for the Crab at the large zenith angle. Differential power index is -2.5.

Chapter 6

Conclusion and Discussion

CANGAROO II, 7m telescope has been started to observe at Woomera, South Australia in May 1999. Since the reflector has a parabolic shape, timing information can be used, and the night sky background is rejected after timing calibrations.

In order to determine the energy thresholds of the 7m telescope for gamma rays and hadrons, each parameter was estimated as follows: reflectivity of mirror was 75 %, light guide efficiency was 60%, hit threshold levels of updating and non-updating discriminator was estimated about 3 photoelectrons and about 4 photoelectrons, which were determined by comparing the single count rate of each PMT for observed data with that expected for the night sky background light.

Using those results, the energy threshold of 7m telescope for hadron shower was estimated to be less than 800 GeV and for gamma-ray was expected to be 200 $\sim$ 300 GeV.

For the purpose of examining the performance of 7m telescope, the Crab Nebula was observed at the large zenith angle with 7m telescope. Total observation times are 39 hours for On-source and 31 hours for Off-source. Here we analyzed 10 hours data observation in January 2000. From the simulated effective area and the spectrum for gamma rays, the threshold energy for gamma rays for the Crab Nebula at the large zenith angle 55° is $\sim$ 1.5 TeV. Gamma-ray signals from the Crab appear as a positive excess around 0° in the alpha distribution of the On-source events against the Off-source events (See 6.1). However, it is not significant statistically. Our analysis for the Crab is on going and all observed data of

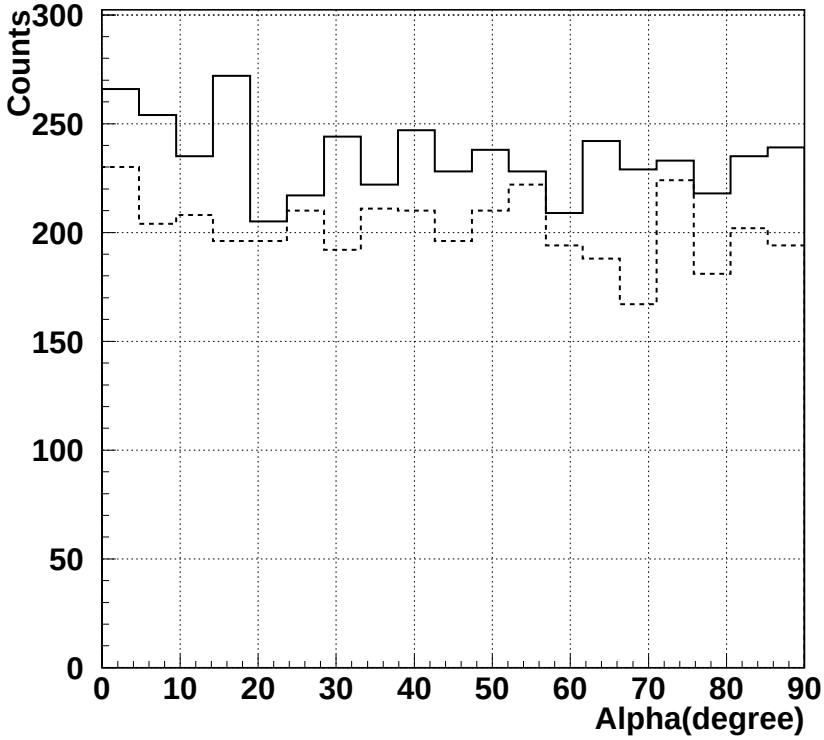

Figure 6.1: Alpha distributions for the Crab Nebula, On-source(solid line) and Off-source(dashed line) using the data from January 2000.

40 hours will be investigated. After analyzing all observed data, more clearly result will be obtained.

At present, we extend 7m telescope reflector to 10m diameter by the additional of 54 more mirrors, and construction of another three 10m telescope are planned (CANGAROO III project). The array of four 10m telescopes for the stereo observation will be completed by 2003. CANGAROO III is expected to be observed in energy range from $\sim$ 100 GeV to 10 TeV and to realize the angular resolution up to $0^{\circ}.05$ for the stereo observations. Therefore, the known gamma-ray sources will be revealed more clearly and more number of gamma-ray sources will become detectable.

Appendix A

Appendix

A.1 Definition of the Image Parameters

Definition of the image parameters used in this thesis is almost the same as of the Hillas parameters originally used in Whipple group. However, the following definition based on the Asymmetry Vector is convenient to make event maps as described in Chapter (). Suppose the i th PMT is given by coordinates (x_i, y_i) in degrees and registers a signal s_i. The following is first defined:

$$\langle x \rangle = \frac{\sum_i s_i x_i}{\sum_i s_i}, \langle y \rangle = \frac{\sum_i s_i y_i}{\sum_i s_i}, \tag{A.1}$$

$$\langle xy \rangle = \frac{\sum_i s_i x_i y_i}{\sum_i s_i}, \langle x^2 y \rangle = \frac{\sum_i s_i x_i^2 y_i}{\sum_i s_i}, \langle xy^2 \rangle = \frac{\sum_i s_i x_i y_i^2}{\sum_i s_i}, \tag{A.2}$$

$$\langle x^2 \rangle = \frac{\sum_i s_i x_i^2}{\sum_i s_i}, \langle y^2 \rangle = \frac{\sum_i s_i y_i^2}{\sum_i s_i}, \langle x^3 \rangle = \frac{\sum_i s_i x_i^3}{\sum_i s_i}, \langle y^3 \rangle = \frac{\sum_i s_i y_i^3}{\sum_i s_i}. \tag{A.3}$$

The coordinates $(\langle x \rangle, \langle y \rangle)$ correspond to the centroid of the image. The following is further defined:

$$\sigma_{x^2} = \langle x^2 \rangle - \langle x \rangle^2, \sigma_{xy} = \langle xy \rangle - \langle x \rangle \langle y \rangle, \sigma_{y^2} = \langle y^2 \rangle - \langle y \rangle^2, \tag{A.4}$$

$$\sigma_{x^3} = \langle x^3 \rangle - 3\langle x^2 \rangle \langle x \rangle + 2\langle x \rangle^3, \sigma_{y^3} = \langle y^3 \rangle - 3\langle y^2 \rangle \langle y \rangle + 2\langle y \rangle^3, \tag{A.5}$$

$$\begin{aligned} \sigma_{x^2y} &= \langle x^2 y \rangle - 2\langle xy \rangle \langle x \rangle - \langle x^2 \rangle \langle y \rangle + 2\langle x \rangle^2 \langle y \rangle, \\ \sigma_{xy^2} &= \langle xy^2 \rangle - 2\langle xy \rangle \langle y \rangle - \langle y^2 \rangle \langle x \rangle + 2\langle y \rangle^2 \langle x \rangle. \end{aligned} \tag{A.6}$$

If $d = \sigma_{y^2} - \sigma_{x^2}$ and $z = [d^2 + 4\sigma_{xy}]^{1/2}$, then

$$\text{Width} = \left(\frac{\sigma_{x^2} + \sigma_{y^2} - z}{2} \right)^{1/2}, \text{ Length} = \left(\frac{\sigma_{x^2} + \sigma_{y^2} + z}{2} \right)^{1/2}. \tag{A.7}$$

If an assumed source position in the field of view is (x_s, y_s) and the Distance vector $\vec{D} = (x_D, y_D)$ is

$$\vec{D} = (x_s - \langle x \rangle, y_s - \langle y \rangle), \tag{A.8}$$

thus

$$\text{Distance} \quad = \quad \sqrt{\langle D \rangle^2 + \langle D \rangle^2}. \tag{A.9}$$

$$\tag{A.10}$$

If an unit vector of the major axis, $\vec{u} = (x_u, y_u)$ is

$$\vec{u} = \left(\left(\frac{z - d}{2z} \right)^{1/2} \text{sign}(\sigma_{\text{xy}}) \left(\frac{\text{z} + \text{d}}{2\text{z}} \right)^{1/2} \right), \tag{A.11}$$

then

$$\text{Alpha} = \cos^{-1} \left(\frac{x_u x_D + y_u y_D}{\text{Distance}} \right). \tag{A.12}$$

And Asymmetry vector $\vec{A} = (x_A, y_A)$ is

$$\vec{A} = -\sigma_A \vec{u}. \tag{A.13}$$

If the largest three PMT signals in the image is S_1 ,S_2 and S_3, Concentration is

$$\text{Conc} \quad = \quad \frac{s_{\text{max}} + s_{\text{2nd}} + s_{\text{3rd}}}{\sum_i s_i}. \tag{A.14}$$

Acknowledgment

I would like to express to my supervisor, Prof. Toru Tanimori my deepest gratitude for good supporting through all this work. I would also like to be grateful to Dr. Hidetoshi Kubo for his helpful advice. I also express my thanks to Prof. Yasushi Watanabe, Prof. Kenji Kaneyuki, Prof. Alex Bondar and Dr. Byung Gu Cheon for their support and encouragement.

I extend my thanks to Prof. Tadashi Kifune for his suggestion. I would also like to thank to Dr. Akiko Kawachi for her good advice and encouragement. I am grateful to Prof. Ryoji Enomoto and Dr. Kimihiro Okumura for giving important comments in this analysis. Thanks are also due to others who assisted me in construction of 7m telescope in Woomera; Prof. Masaki Mori, Prof. Kyoshi Nishijima, Prof. J.R.Patterson, Prof. Shohei Yanagita, Dr. Takanori Yoshikoshi, Mr.Jun'ichiro Jimbo, and staffs of Mitsubihi Electric Corporation. I express my thanks to all other members of the CANGAROO group.

I would like to thank all of my colleagues in Watanabe-Tanimori laboratory; Dr. Atsuhiko Ochi, Dr. Yasunobu Oshima, Dr. Koji Sakurazawa, Mr. Shunsuke Ichizawa, Mr. Yuji Nishi, Ms. Masayo Moriya, Mr. Migaku Ohta, Mr. Hidekazu Kakuno, Mr. Jun'ichi Kaneko, Mr. Satoshi Hara, Mr. Takahiro Futagami, Mr. Atsushi Namekata, Mr. Hiroshi Fujiyasu, Mr. Akihiro Asahara, Mr. Kazuyoshi Takano, Mr. Tomohiro Nakamura, Mr. Tsutomu Nagayoshi, Mr. Toshihisa Hirai, Mr. Mikio Morii, Ms. Reiko Orito, Mr. Satoshi Koishi, Mr. Hiroshi Nishihama, and Mr. Shotaro Yanaka for their support and encouragement.

And I would like to thank to all who supported me to complete this work.

Bibliography

[1] Aharonian F., et al., *Towards a Major Atmospharic Cherenkov Detector III., Tokyo*, 1994.

[2] Baltrusaitis,r.m.,et al., *Nucl. Inst. Meth. Phys. Res. A, 240, 410-428*, 1985.

[3] Hillas, A.M. *J. Phys. G 8* , 1982.

[4] Hillas, A.M. *Proc. 19th ICRC., La Jolla, 3, 445-448*, 1985.

[5] Hillas, A.M.et al, *Astrophys, J. 503, 744-759*, 1998.

[6] Jelley, J. V., *Čerenkov Radiation and its Applications*, 1958, Pergamon Press. p219.

[7] MacKeown, P.K., et al., *Proc. 18th ICRC., Bangalore, 9, 175-178*, 1983.

[8] M. Punch, *PhD thesis, NAional University of Ireland*, 1993.

[9] P. Sommers., et al., *J. Phys. G, 13, 553*, 1987.

[10] R.Burn., et al., *GEANT3 Users Guide, CERN DD/EE/84-1*,

[11] Thompson,D.J. et al, *The Third EGRET Catalog of High-Energy Gamma-Ray Sources*, (http://cossc.gsfc.nasa.gov/cossc/egret/egret_doc.html)

[12] NASA. *Chandra X-ray Obervatory Center*, (http://chandra.harvard.edu/index.html)

[13] T. Hara, et al., *Nucl. Inst. Meth. Phys. Res. A, 332,300-309*, 1993.

[14] A.Kawachi., *Prec. 26th ICRC., Salt Lake City*, 1999.

[15] A.Kawachi. et al., *will be sibitted in Astroparticle Physics*, 2000.

[16] H.Kubo. et al., *Towards a Major Atmospharic Cherenkov Detector VI., Snowbird*, 1999.

[17] M. Mori. et al., *Prec. 26th ICRC., Salt Lake City*, 1999.

[18] K. Sakurazawa. et al., *Prec. 25th ICRC., Durban, 3, 165-168*, 1997.

[19] T. Tanimori, et al., *Towards a Major Atmospharic Cherenkov Detector III., Tokyo*, 1994.

[20] T. Tanimori, et al., *Prec. 26th ICRC (Salt Lake City)*, 1999.

[21] S. Gunji, *CANGAROO-II observation manual V1.0*, 1999.

[22] S. Hara, *Master's thesis*,Tokyo Institude of Technology, 1999.

[23] S. Kamei, *Master's thesis*,Tokyo Institude of Technology, 1998.

[24] M. Moriya, *PhD thesis*,Tokyo Institude of Technology, 2000.

[25] R. Susukita, *PhD thesis*, Kyoto University, 1997.

[26] K. Sakurazawa, *PhD thesis*,Tokyo Institude of Technology, 1999.

[27] T. Tsukakoshi *Master's thesis*,Tokyo Institude of Technology, 1994.

[28] T. Yoshikoshi, *Master's thesis*,Tokyo Institude of Technology, 1993.

[29] T. Yoshikoshi, *PhD thesis*,Tokyo Institude of Technology, 1996.